

**HEAT TRANSFER AND PRESSURE DROP FOR FLOW OF
SUPERCritical AND SUBCRITICAL CO₂
IN MICROCHANNEL TUBES**

Final Technical Report
by

Jostein Pettersen, René Rieberer, Svend Tollak Munkejord
February, 2000

for
United States Army
EUROPEAN RESEARCH OFFICE OF THE U.S.ARMY
London, England

CONTRACT NUMBER N-68171-99-M-5674

R&D no: 8665-CH-01.

SINTEF Energy Research / Norwegian University of Science and Technology
Department of Refrigeration and Air Conditioning
Kolbjørn Hejes vei 1D
N-7465 Trondheim, NORWAY
Contact e-mail: Jostein.Pettersen@energy.sintef.no

Approved for Public Release; distribution unlimited

DTIC QUALITY INSPECTED 4

20000616 053

REPORT DOCUMENTATION PAGE

Form Approved
OMB NO. 0704-0188

Public Reporting burden for this collection of information is estimated to average 1 hour per response, including the time for reviewing instructions, searching existing data sources, gathering and maintaining the data needed, and completing and reviewing the collection of information. Send comment regarding this burden estimates or any other aspect of this collection of information, including suggestions for reducing this burden, to Washington Headquarters Services, Directorate for Information Operations and Reports, 1215 Jefferson Davis Highway, Suite 1204, Arlington, VA 22202-4302, and to the Office of Management and Budget, Paperwork Reduction Project (0704-0188) Washington, DC 20503.

1. AGENCY USE ONLY (Leave Blank)		2. REPORT DATE February 9, 2000	
		3. REPORT TYPE AND DATES COVERED FINAL REPORT, MARCH 1999 – FEBRUARY 2000	
4. TITLE AND SUBTITLE Heat Transfer and Pressure Drop for Flow of Super-critical and Sub-critical CO ₂ in Microchannel Tubes		5. FUNDING NUMBERS C N-68171-99-M-5674	
6. AUTHOR(S) JOSTEIN PETTERSEN, RENÉ RIEBERER, SVEND TOLLAK MUNKEJORD			
7. PERFORMING ORGANIZATION NAME(S) AND ADDRESS(ES) SINTEF Energy Research / Norwegian University of Science and Technology Department of Refrigeration and Air Conditioning Kolbjørn Hejes vei 1D N-7465 Trondheim, NORWAY		8. PERFORMING ORGANIZATION REPORT NUMBER TR A5127	
9. SPONSORING / MONITORING AGENCY NAME(S) AND ADDRESS(ES) DEFENSE FINANCE AND ACCOUNTING SER Rock Island Operating Location Rock Island, IL 61299-8401		10. SPONSORING / MONITORING AGENCY REPORT NUMBER	
11. SUPPLEMENTARY NOTES			
12 a. DISTRIBUTION / AVAILABILITY STATEMENT		12 b. DISTRIBUTION CODE	
13. ABSTRACT (Maximum 200 words) Within this project, the heat transfer and pressure drop characteristics of CO ₂ (R-744) were investigated at supercritical pressures (cooling) and subcritical pressures (evaporation). The measurements were carried out with a microchannel type (MPE) tube with 25 parallel ports and a port diameter of 0.787 mm. The experimental data collected confirm that CO ₂ offers high heat transfer coefficients at supercritical pressures. The comparison of these data with common correlations shows good correspondence. The comparison of the measured pressure drop data with calculation models is satisfactory as well. At evaporation the situation is not as clear. The experiments at high mass fluxes have shown a strongly decreasing heat transfer coefficient from a certain vapour fraction upwards. A comparison with a calculation model for dry-out has shown that this drop has to be expected. On the contrary, at low mass fluxes no influence of the velocity was detected. None of the heat transfer calculation models investigated takes this phenomenon into account. The two-phase pressure drop correlations yield too low values in general, but for a first estimation models from the literature can be taken.			
14. SUBJECT TERMS CO ₂ , R-744, Heat Transfer, Pressure Drop, Multiport Extruded Tubes, Supercritical, Subcritical		15. NUMBER OF PAGES 81 (incl. Cover Page)	
		16. PRICE CODE	
17. SECURITY CLASSIFICATION OR REPORT UNCLASSIFIED	18. SECURITY CLASSIFICATION ON THIS PAGE UNCLASSIFIED	19. SECURITY CLASSIFICATION OF ABSTRACT UNCLASSIFIED	20. LIMITATION OF ABSTRACT UL

NSN 7540-01-280-5500

Standard Form 298 (Rev.2-89)
Prescribed by ANSI Std. Z39-18
298-102

Table of Contents

<u>1 INTRODUCTION</u>	<u>1</u>
1.1 OBJECTIVES	1
1.2 BACKGROUND	1
1.3 THIS REPORT	3
1.4 ACKNOWLEDGEMENTS	3
<u>2 BASIC HEAT TRANSFER AND PRESSURE DROP CORRELATIONS</u>	<u>5</u>
<u>3 TEST FACILITIES</u>	<u>13</u>
3.1 OVERVIEW	13
3.2 COMPONENTS	17
3.2.1 TEST SECTION	17
3.2.2 REFRIGERANT PUMP	18
3.2.3 COOLANT PUMPS	18
3.2.4 BYPASSES	18
3.3 MEASUREMENT EQUIPMENT	18
3.3.1 TEMPERATURE	18
3.3.2 PRESSURE	19
3.3.3 MASS FLOW	19
3.3.4 ELECTRICAL POWER	19
3.3.5 DATA LOGGING AND PROCESSING	19
<u>4 WILSON PLOT CALIBRATION</u>	<u>21</u>
4.1 PRINCIPLES OF THE WILSON PLOT METHOD	21
4.2 RESULTS OF THE WILSON PLOT	26
4.2.1 WATER HEATING	26
4.2.2 WATER COOLING	27
4.2.3 COMPARISON OF THE WILSON PLOTS	28
<u>5 RESULTS</u>	<u>31</u>
5.1 SUPERCRITICAL CONDITIONS (COOLING)	31
5.1.1 GENERAL	31
5.1.2 HEAT TRANSFER AT SUPER-CRITICAL PRESSURES	33
5.1.3 PRESSURE DROP AT SUPER-CRITICAL PRESSURES	39
5.2 SUBCRITICAL CONDITIONS (EVAPORATION)	43
5.2.1 GENERAL	43
5.2.2 HEAT TRANSFER AT EVAPORATION	44
5.2.3 PRESSURE DROP AT EVAPORATION	53
<u>6 ASSESSMENT OF RESULTS</u>	<u>57</u>
6.1 PREVIOUS EVAPORATOR MEASUREMENTS	57
6.2 EVAPORATOR SIMULATIONS	58
6.3 DISCUSSION	59
<u>7 CONCLUSIONS</u>	<u>61</u>
<u>BIBLIOGRAPHY</u>	<u>63</u>
<u>NOMENCLATURE</u>	<u>67</u>

APPENDIX : CORRELATIONS	71
A.1 SUPER-CRITICAL CONDITIONS (COOLING)	71
A.1.1 HEAT TRANSFER	71
A.1.2 PRESSURE DROP	72
A.2 SUB-CRITICAL CONDITIONS (EVAPORATION)	72
A.2.1 HEAT TRANSFER	72
A.2.2 PRESSURE DROP	73

1 INTRODUCTION

1.1 Objectives

The technical objectives of the present project were:

1. to obtain experimental data for heat transfer coefficients for flow of carbon dioxide (CO₂, R-744) in a micro-channel tube, with an inner diameter of approximately 0.8 mm, under relevant conditions for compact gas coolers and evaporators in CO₂-based air conditioning systems.
2. to obtain experimental data for pressure drop gradients for flow of carbon dioxide in micro-channel tubes, with an inner diameter of approximately 0.8 mm, under relevant conditions for compact gas coolers and evaporators in CO₂-based air conditioning systems.
3. to assess the consequences of the measured data regarding design of compact heat exchangers for CO₂-based air conditioning systems. Of particular interest is the assessment of reversible heat exchangers for cooling/heating operation.
4. to enable the US Army to accelerate the development of efficient heat exchangers for CO₂ air conditioning and heat pump units.

Operation near the critical point (31.1°C/73.8 bar) is expected to affect heat transfer characteristics of CO₂. Earlier measurements indicate effects on heat transfer from property variations (wall-bulk variation, buoyancy effects) near pseudo-critical points at super-critical pressures, as well as nucleate boiling regimes with improved heat transfer for evaporation at near-critical pressures [1]. There is considerable uncertainty about the validity of pressure drop correlations developed for larger diameter tubes when used for modelling small-diameter tube flow, especially during evaporation.

1.2 Background

Chlorine-containing CFC and HCFC refrigerants used in civil and military air conditioners are now being phased out due to their ozone depleting effect. The fluorocarbon chemical industry is offering chlorine-free HFC fluids as replacement refrigerants, but these fluids still have considerable global warming impact, and strict measures will have to be introduced to prevent escape of refrigerant to the atmosphere. These measures will include mandatory systems/procedures for recycling and recovery that may seriously impact the logistics in military

operations. There is also some uncertainty about long-term health and environmental effects of these man-made chemicals. Another approach for developing sustainable CFC/HCFC-free technology is to use naturally occurring fluids as refrigerants [3]. This is a relatively new area of research that is now gaining interest especially in Europe. For obvious reasons, these developments do not enjoy the support of the fluorocarbon industry.

The natural refrigerant carbon dioxide (CO₂, R-744) has recently been "rediscovered" as a possible vapour compression working fluid [4], [5], mainly due to its unique combination of ecological and personal safety. CO₂ is a non-toxic and non-combustible natural fluid that offers full environmental safety. It is widely available in sufficient quantities and at a very reasonable cost all over the world, and there is no need to recover or recycle it. The thermodynamic and transport properties of CO₂ are quite different from those of conventional refrigerants. As a consequence, novel cycles and circuiting concepts, new control schemes [6] and redesigned components (compressors, heat exchangers) need to be developed.

A number of research and development projects on CO₂-based vapour compression systems are now in progress, focusing on applications such as motor vehicle air conditioning systems [4] and heat pumps [7], hot water heat pumps [8], residential/commercial air conditioning/heat pumps [9], and various refrigeration areas. The common goal for these projects is to determine or demonstrate the practical potential of CO₂ systems. The Norwegian University of Science and Technology (NTNU) and its contract research foundation SINTEF has conducted extensive research in this area since 1988, and is one of the leading laboratories in the world on CO₂ air conditioning technology.

In the USA, the Environmental Systems Branch of the CECOM RD&E Center has initiated investigations related to CO₂ air-conditioning units for the US-Army [10]. The goal is to develop smaller and lighter packaged A/C or HVAC units for military applications, using the environmentally neutral refrigerant CO₂.

The weight and volume of heat exchangers built with MultiPort Extruded (MPE) aluminium micro-channel tubes can be reduced compared to conventional tube/fin heat exchangers with mechanically expanded round tubes. This present project was aimed at basic research on heat transfer coefficients and pressure drop data inside MPE tubes with CO₂ as the refrigerant, and the resulting impact on heat exchanger design. The results of this project will be data that can be used for design optimisation of MPE tube heat exchangers [11]. This design optimisation will focus on heat exchanger performance as well as size and mass reduction.

Based on extensive communication between NTNU/SINTEF and the Environmental Systems Branch of CECOM RD&E Center (John Manzione), it was decided to apply for Seed Project funding from ERO to establish R&D Cupertino, and start the research necessary for developing a new generation of CO₂-based Environmental Control Units.

1.3 This report

This report presents the results of the investigations. The contents are:

- Chapter 1: Basic correlations for heat transfer and pressure drop
- Chapter 2: Description of the test facilities at the laboratory of SINTEF-NTNU
- Chapter 3: Background of the Wilson Plot calibration which is used to find a reliable correlation of the water-side heat transfer coefficient
- Chapter 4: Shows the results of the heat transfer and pressure drop measurements
- Chapter 5: Summarises the main results
- Chapter 6: Gives a brief assessment of the implications of the measurement data on evaporator design

The Appendix contains recommended correlations for heat transfer and pressure drop of CO₂ in the MPE tube.

1.4 Acknowledgements

It has to be stated that Mr. Andreas Leister has carried out most of the experiments within his diploma work at SINTEF Energy Research [1]. His contribution is gratefully acknowledged.

The project was sponsored jointly by the European Research Office, London, and the CECOM Research, Development, and Engineering Center of the U.S. Army at Ft. Belvoir, Virginia.

2 BASIC HEAT TRANSFER AND PRESSURE DROP CORRELATIONS

The following text outlines some basic equations for heat transfer and pressure drop which are used in order to obtain the experimental results presented in Chapter 5. Here, largely the same approach is used as in [25].

The heat transfer coefficient is defined as

$$\alpha = \frac{\dot{q}}{\Delta T}, \quad (1)$$

where \dot{q} is the heat flux according to

$$\dot{q} = \frac{\dot{Q}}{A}. \quad (2)$$

\dot{Q} is the heat transfer rate and A is the heat transfer area, i.e. the tube wall surface, ΔT refers to the local temperature difference between the fluid (T) and the wall (T_w):

$$\Delta T = |T - T_w|, \quad (3)$$

Unfortunately it is not as easy as it seems to measure this temperature difference between the bulk and the wall surface, because high heat transfer coefficients lead to small temperature differences to measure. Furthermore, it is difficult to place temperature sensors in small tubes, especially in a MultiPort Extruded (MPE) tube. Therefore, another method was applied to determine the heat transfer coefficient of the refrigerant. The procedure is based on the heat exchange between CO_2 and a 'secondary' fluid (water). The following paragraphs give an introduction to the heat transfer process in a heat exchanger.

Figure 1 shows a small cell of a counter-flow heat exchanger with the length Δl . In the following, Δl is assumed to be small, thus all fluid properties and the heat transfer coefficient may be considered constant.

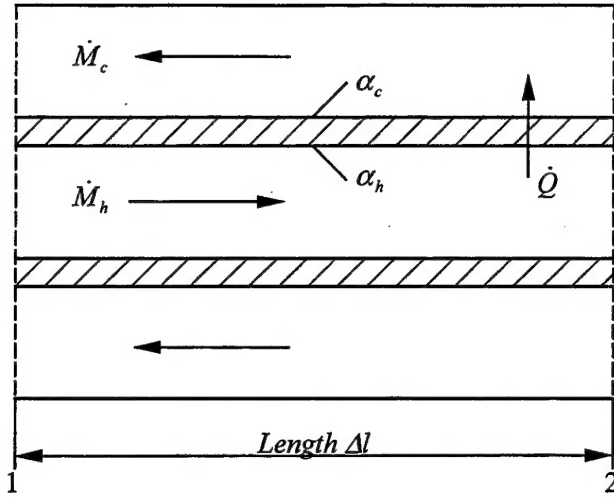


Figure 1: A model of a small counter-flow heat exchanger cell

The index 'c' refers to the cold fluid and 'h' to the hot fluid. The hot fluid enters the element at point 1 and leaves it at point 2 while the cold fluid enters at 2 and leaves 1.

Because of the first law of thermodynamics in an ideally insulated heat exchanger the heat delivered by the hot fluid

$$\dot{Q} = \dot{M}_h \cdot (h_{h,1} - h_{h,2}), \quad (4)$$

must be equal to the heat absorbed by the cold fluid:

$$\dot{Q} = \dot{M}_c \cdot (h_{c,2} - h_{c,1}), \quad (5)$$

Now, it is necessary to combine the heat exchanged with the overall heat transfer coefficient:

$$\dot{Q} = k \cdot A_h \cdot \Delta T_{lm}. \quad (6)$$

where k is the overall heat transfer coefficient based on the heat transfer surface on the hot side (A_h):

$$\frac{1}{k} = \frac{1}{\alpha_h} + R_w + \frac{A_h}{\alpha_c \cdot A_c}. \quad (7)$$

A_c is the heat transfer surface on the cold side, which is here the outer side. The heat transfer resistance (R_w) in the tube wall is based on the inner tube area. The possible existence of fouling layers is disregarded.

As stated above, a small heat exchanger element is considered in which all properties and even the temperatures are constant. Since the present test section is not as small, the temperatures change. Therefore, it is necessary to replace the (local) temperature difference by the mean temperature difference, the logarithmic mean temperature difference (ΔT_{lm}) [14]:

$$\Delta T_{lm} = \frac{\Delta T_1 - \Delta T_2}{\ln\left(\frac{\Delta T_1}{\Delta T_2}\right)} \quad (8)$$

with

$$\Delta T_1 = T_{h,1} - T_{c,1} \quad \text{and} \quad \Delta T_2 = T_{h,2} - T_{c,2}. \quad (9)$$

Equation (8) requires constant properties of both fluids and a constant overall heat transfer coefficient. The first condition was not generally fulfilled. In particular for the single-phase experiments, the gliding temperature on the CO₂-side caused the specific heat capacity c_p to vary significantly, especially in the vicinity of the (pseudo-) critical point. Therefore, the following approach was used instead to obtain a mean temperature difference from which to calculate the overall heat transfer coefficient: In the calculation, the test section was divided into 60 cells i of equal heat exchange \dot{Q}_i . Using the measured inlet and outlet conditions, as well as an assumption that the pressure decreased linearly with the exchanged heat (see [15]), the temperature profile of each fluid could be calculated. Thus the temperature T_i of each cell was known. Rewriting equation (6) for cell i yields

$$(kA)_i = \frac{\dot{Q}_i}{\overline{\Delta T}_i}. \quad (10)$$

where A_i is the CO₂-side area necessary to exchange the heat in cell i and $\overline{\Delta T}_i$ is the mean temperature difference between the hot and the cold fluid of cell i . It was inherent in the design of the experiment that the overall heat transfer coefficient k was assumed to be constant. Now it could be calculated by summing equation (10) over all the cells N , and dividing by the known total CO₂-side area, A_h :

$$k = \frac{1}{A_h} \sum_{i=1}^N (kA)_i . \quad (11)$$

As shown above, the overall heat transfer is given by the heat transfer coefficients on the hot and the cold side and the (known) heat transfer resistance in the wall. If one of the heat transfer coefficients (α_h or α_c) is known, it is possible to determine the unknown (α_c or α_h). In the present tests, water flows on the outer side of the tube and the refrigerant (CO_2) flows on the inner side. In order to find an equation for the single-phase heat transfer coefficient of the water the so-called Wilson-Plot method was used. This method is described in Chapter 4. By means of this value, the (re-)calculation of the heat transfer coefficient on the CO_2 -side can be easily done if the conditions of both fluids at the inlet are known.

The second part of the present work was to determine the pressure drop of the refrigerant in the MPE tube along the heat transferring length. Friction and acceleration/deceleration of the refrigerant cause this drop. The design of the test section allows only the measurement of the total pressure drop between the manifolds and not the measurement of the pressure drop along the heat transfer length (Figure 2 and see Chapter 3). Therefore, it was necessary to do some assumptions.

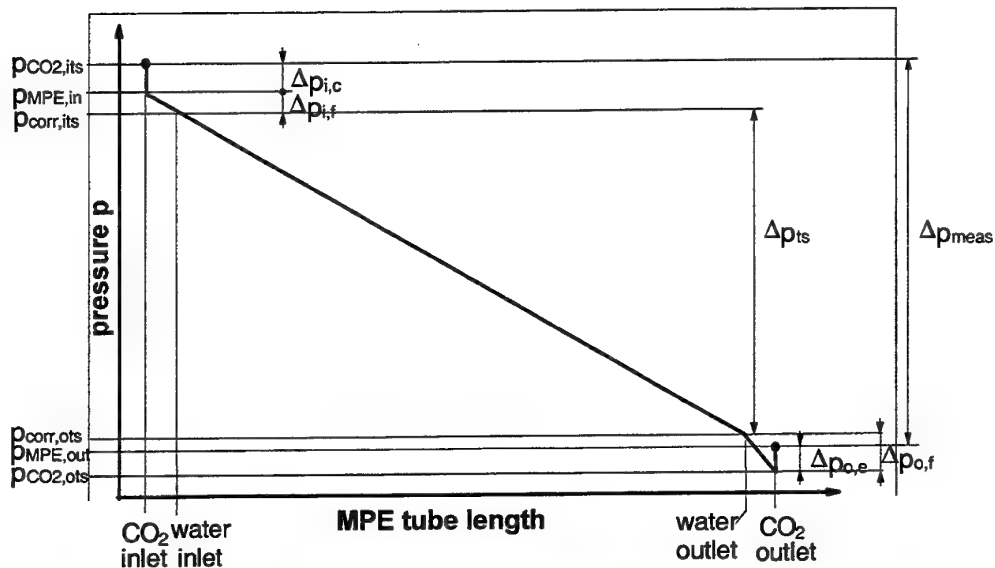
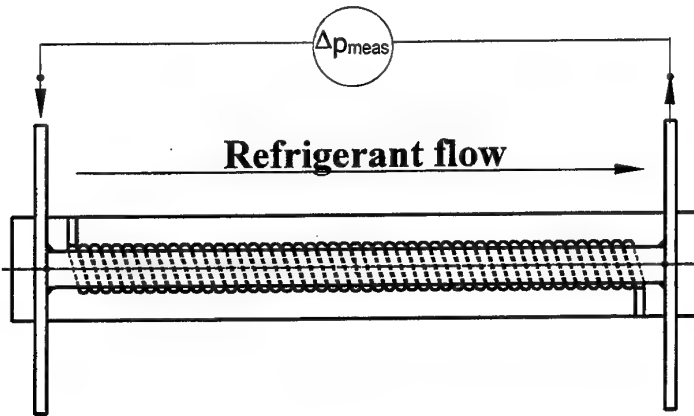


Figure 2: Sketch of the MPE tube (with water channels) and refrigerant pressure along the tube (simplified)

While flowing from the manifold into the MPE tube – consisting of 25 parallel ports - a sudden contraction occurs to the refrigerant. This leads to a pressure drop at the inlet. At the outlet of the MPE tube the opposite effect occurs. An expansion leads to a pressure rise. Calculation models for these pressure changes are described in [17] and [19] ([15]):

In case of a single-phase flow the contraction pressure drop at the inlet is given by

$$\Delta p_{i,c} = \frac{\dot{m}^2}{2 \cdot \rho} \cdot (1 - \sigma^2 + K_c). \quad (12)$$

The pressure rise due to expansion at the outlet can be calculated according to

$$\Delta p_{o,e} = \frac{\dot{m}^2}{2 \cdot \rho} \cdot (1 - \sigma^2 - K_e). \quad (13)$$

Where \dot{m} is the mass flux of the fluid in the ports and σ is the ratio of the total port area ($A_{p,tot}$) and the front area (A_{fr}) of the MPE tube. For the present test tube it is

$$\sigma = \frac{A_{p,tot}}{A_{fr}} = 0.28 \quad (14)$$

The entrance and exit pressure loss coefficients (K_c and K_e) are also a function of the contraction and expansion geometries and in some cases of the Reynolds number. Kays and London determined them. For turbulent flow with an approximate Reynolds number of 10,000 and the geometry of the used tube these factors are

$$K_c = 0.4 \text{ and } K_e = 0.5. \quad (15)$$

In case of a two-phase flow, the models for the effects at the inlet and the outlet are more complicated ([18],[19]). The inlet pressure drop caused by the sudden contraction can be written as

$$\Delta p_{i,c} = \left(\frac{\dot{m}}{C_c} \right)^2 \cdot (1 - C_c) \cdot \left\{ \frac{(1 + C_c) \cdot \left(\frac{x^3 \cdot v_g^2}{\varepsilon^2} + \frac{(1-x)^3 \cdot v_l^2}{(1-\varepsilon)^2} \right)}{2 \cdot [x \cdot v_g + (1-x) \cdot v_l]} - C_c \cdot \left(\frac{x^2 \cdot v_g}{\varepsilon} + \frac{(1-x)^2 \cdot v_l}{(1-\varepsilon)} \right) \right\} \quad (16)$$

and the outlet pressure rise:

$$\Delta p_{o,e} = \dot{m} \cdot \sigma \cdot (1 - \sigma) \cdot v_l \cdot \left\{ \frac{(1-x)^2}{(1-\varepsilon)} + \left(\frac{v_g}{v_l} \right) \cdot \frac{x^2}{\varepsilon} \right\} \quad (17)$$

As can be seen from the equations (16) and (17), there are two new parameters, the coefficient of contraction (C_c) and the void fraction (ε):

C_c depends on the contraction ratio already defined by equation (14). For the present installation, the coefficient becomes

$$C_c \approx 0.6 \quad (18)$$

The void fraction can be calculated as

$$\varepsilon = \left[1 + \frac{1-x}{x} \cdot \left(\frac{\rho_g}{\rho_l} \right)^{\frac{2}{3}} \right]^{-1} \quad (19)$$

The refrigerant also flows through two short sections at the ends of the tube where no heat is transferred. The frictional pressure drop occurring in these adiabatic parts of the MPE tube may be calculated by means of the Blasius friction factor

$$f = \frac{0.3164}{Re^{0.25}} \quad (20)$$

and the general form for the pressure drop:

$$\Delta p_f = f \cdot \frac{\Delta l}{d} \cdot \frac{\dot{m}^2}{2 \cdot \rho} \quad (21)$$

In case of two-phase flow, the adiabatic pressure drop may also be calculated using the Blasius friction factor but using an equivalent mass flux for the liquid phase (\dot{m}_{eq}) instead of the total mass flux (\dot{m}) [20]:

$$\dot{m}_{eq} = \dot{m} \cdot \left\{ (1-x) + x \cdot \left(\frac{\rho_l}{\rho_g} \right)^{\frac{1}{2}} \right\} \quad (22)$$

With these equations the 'adiabatic' pressure drop at the inlet ($\Delta p_{i,f}$) and at the outlet ($\Delta p_{o,f}$) can be calculated.

Finally, the pressure drop occurring along the heat transferring length of the test section (Δp_{ts}) can be calculated according to

$$\Delta p_{ts} = \Delta p_{meas} - \Delta p_{i,c} - \Delta p_{i,f} - \Delta p_{o,f} + \Delta p_{o,e} \quad (23)$$

Note that because of the horizontal installation of the MPE tube, there is no influence of gravity.

3 TEST FACILITIES

This chapter gives an overview of the test rig for measuring heat transfer and pressure drop data of CO₂ in MPE tubes at the laboratory of SINTEF – NTNU in Trondheim, Norway.

3.1 Overview

The test rig consisted of three main parts:

- the refrigerant loop,
- the test section, and
- the “coolant” (water) loop ¹

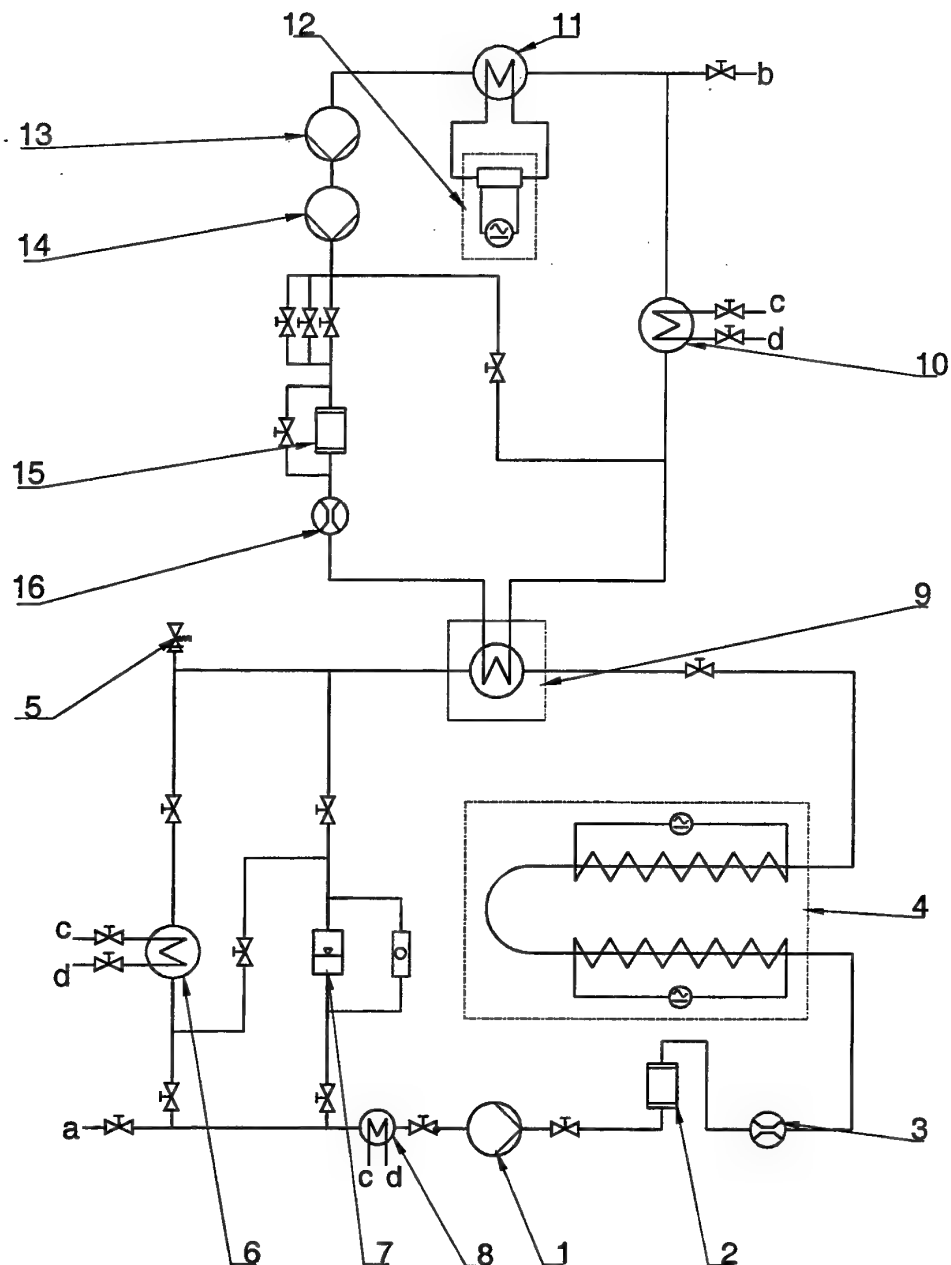
Figure 3 shows the flow circuit of the test rig that allowed the analysis of the heat rejection process of CO₂ at super-critical pressures (single-phase cooling, ‘gas cooling’) and the heat absorption process at sub-critical pressures (evaporation) in MPE tubes (Figure 7, Figure 8). The refrigerant flow through the system depended on the process to be analyzed. Figure 4 a) shows the refrigerant flow at cooling tests and Figure 4 b) at evaporation tests. The following system description is based on the cooling tests. Afterwards the main differences for the evaporation tests are pointed out briefly.

Cooling Tests

For testing super-critical CO₂, the desired pressure in the test rig was set with an electrically heated CO₂ cylinder. This cylinder was connected to the system at (a). Refrigerant was circulated through the system by means of a gear pump (1). It entered the pre-heat section (4) where heat was added electrically, thus the refrigerant state could be set to the desired test conditions, i.e. heated up to the desired temperature. The refrigerant then entered the test section (9) where heat exchange between the refrigerant and the coolant took place. After exiting the test section, the refrigerant entered the refrigerant condenser (6), where was removed.

Figure 5 shows the measurement points of the refrigerant loop, which included a Coriolis-type mass flow meter (\dot{M}_{ref}), pressure and temperature measurements at the preheat section inlet ($t_{ref,ips}$, $p_{ref,ips}$), temperature between the upper and lower preheat section ($t_{ref,mps}$), temperature and the pressure at the test section inlet ($t_{ref,its}$, $p_{ref,its}$), temperature at the test section outlet ($t_{ref,ots}$), and pressure drop across the test section (Δp_{ref}). The cooling fluid temperature ($t_{con,o}$) was also measured.

¹ Although water is used as heat source and as heat sink the expression coolant loop is used here.



Refrigerant loop:

- 1 Refrigerant pump
- 2 Refrigerant filter
- 3 Refrigerant mass flow meter
- 4 Pre-heat section
- 5 Safety valve (102 bar)
- 6 Refrigerant condenser

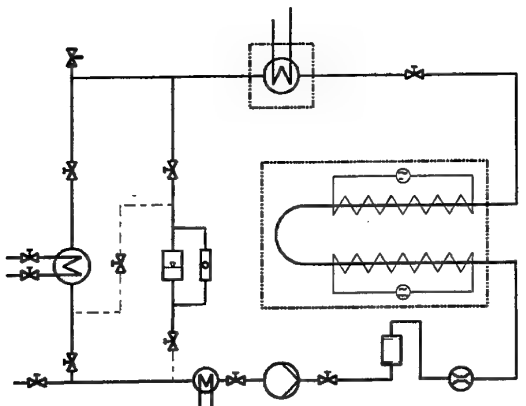
7 Refrigerant receiver with sight glass

- 8 'Sub-cooler'
- Test section:**
- 9 Test section
- Coolant loop:**
- 10 Coolant cooler
- 11 Coolant tank with heat exchanger
- 12 Water heater (Type HAAKE)

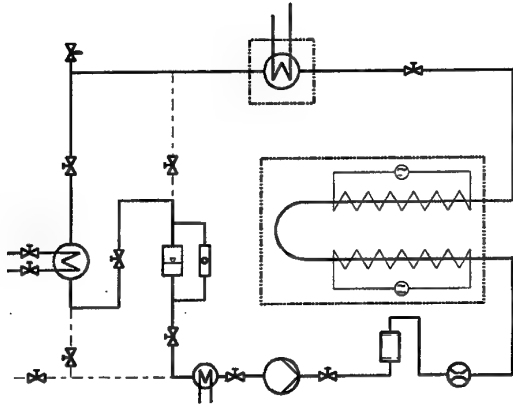
13 Main coolant pump

- 14 Booster coolant pump
- 15 Coolant filter
- 16 Coolant mass flow meter
- Supply lines:**
- a Refrigerant charge
- b Coolant charge
- c City water inlet
- d City water outlet

Figure 3: Flow chart of the MPE tube test rig



a) refrigerant flow at gas cooling tests



b) refrigerant flow at evaporation tests

Figure 4: Flow of the refrigerant through the system at cooling and evaporation tests

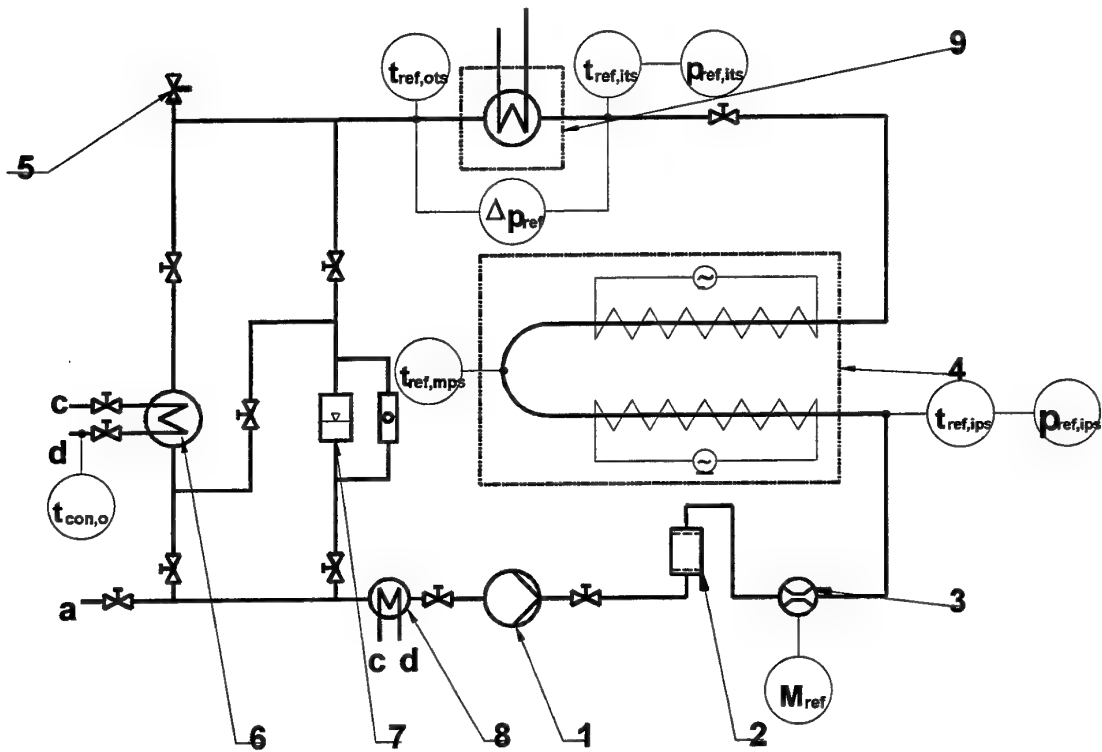


Figure 5: Refrigerant loop with measurement points (component no. see Figure 3)

The coolant loop with the measurement points is shown in Figure 6. As can be seen, after exiting the test section (9) the heated coolant flowed through a heat exchanger (10) where it was cooled down. In the following coolant tank (11) the coolant could be heated to a defined temperature with a water heater of the type HAAKE (12), thus the desired coolant temperature could be set.

Two centrifugal pumps (13 and 14) circulated the coolant through the loop and by means of varying the opening of the bypasses the flow rate could be varied.

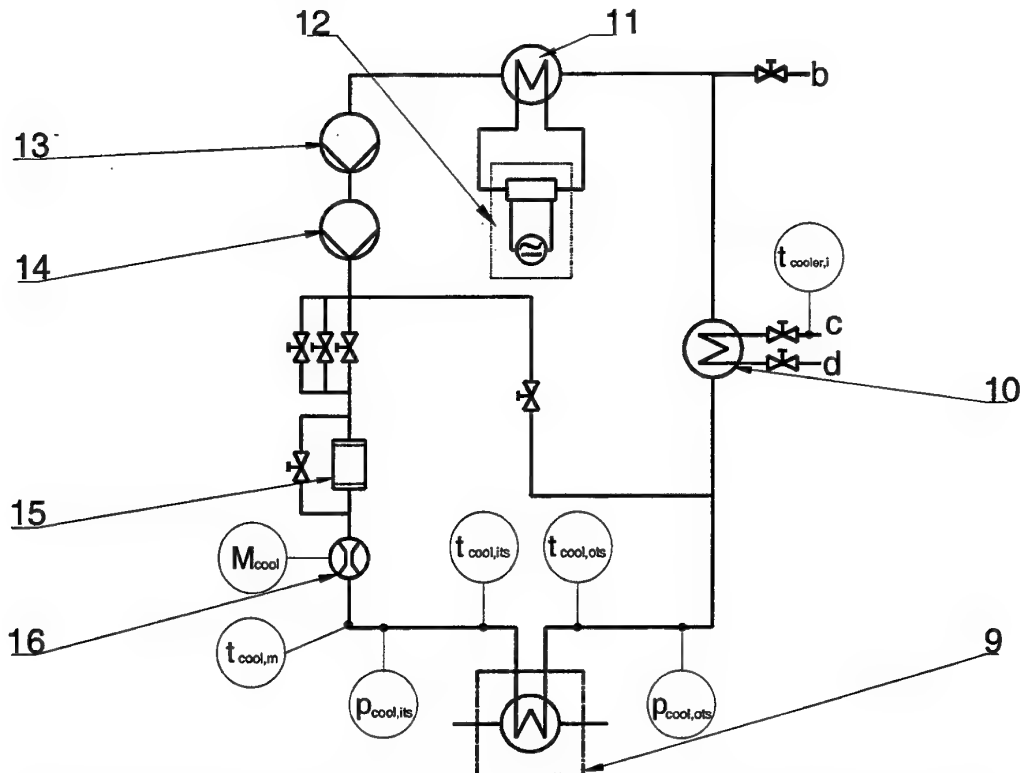


Figure 6: Coolant loop with measurement points (component no. see Figure 3)

The mass flow rate (\dot{M}_{cool}) was measured with a Coriolis-type mass flow meter (16). Temperatures and pressures at the test section inlet and outlet ($t_{cool,its}$; $t_{cool,ots}$; $p_{cool,its}$; $p_{cool,ots}$) were also measured. Close to the mass flow meter, the temperature of the coolant ($t_{cool,m}$) was measured. Another measured temperature was the coolant temperature at the cooler inlet ($t_{cooler,i}$).

Evaporation Tests

The main adjustment necessary to run the evaporation tests was the change of the cooling fluid used in the CO_2 condenser (6), because temperatures below 0°C were necessary (down to about -15°C). Ethanol cooled by a HAAKE COOLER was used for evaporation tests instead of city water.

Refrigerant flow through the system in evaporation tests was also different. It is shown in Figure 4 b). To obtain the desired saturation pressure of the refrigerant, the refrigerant leaving the condenser flowed through the vessel (7) before it reached the pump. The refrigerant charge had to be chosen in such a way that during the tests, a liquid level could be seen in this vessel, i.e. the refrigerant left the condenser in saturated liquid state. To avoid cavitation in the refrigerant pump located after the vessel, the refrigerant had to be cooled down (sub-cooling of about 3 K). For this purpose a small heat exchanger (8) was installed.

3.2 Components

3.2.1 Test Section

The MPE tube to be investigated was a 540 mm long tube soldered in manifolds on both ends. The cross-section of the MPE tube can be seen in Figure 7. The tube was made of a zinc-coated aluminium tube with 25 round ports each with a diameter of 0.787 mm (manufactured by HYDRO ALUMINIUM ADRIAN).

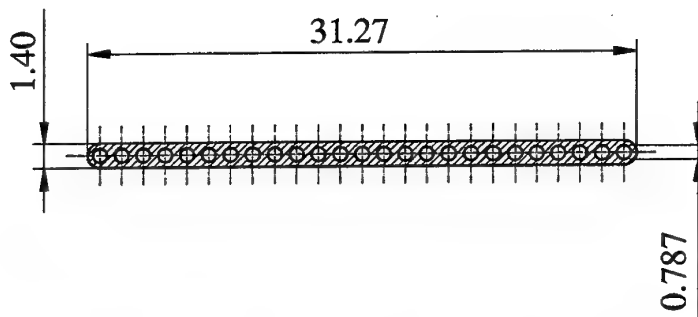


Figure 7: Cross-section of the multiport extruded (MPE) tube

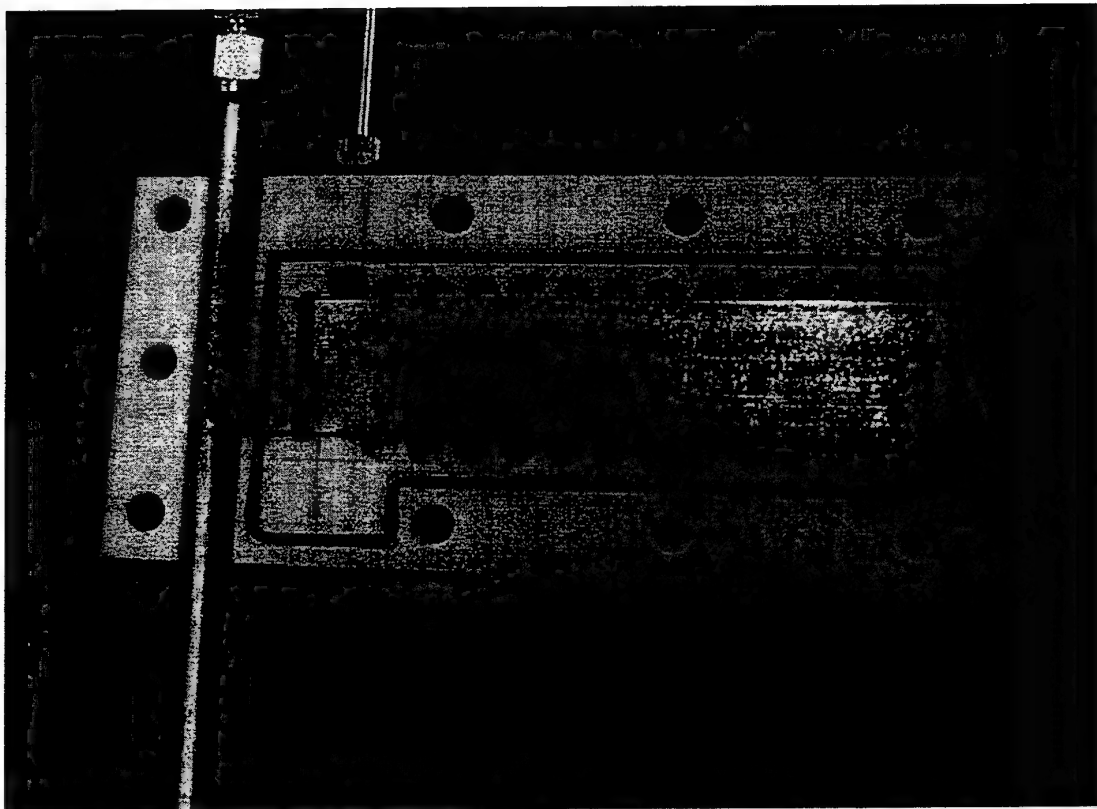


Figure 8: Photograph of the MPE test tube with manifold lying in the (opened) Teflon jacket

The test tube was placed inside a PFTE (Teflon) jacket, where the coolant channels were milled out. These channels were shaped like an edgy double helix around the MPE tube. A photograph

of the MPE tube laying in the (opened) PFTE jacket is shown in Figure 8. The outside of the jacket was insulated with 25 mm thick plates of polystyrene (STYROFOAM).

3.2.2 Refrigerant Pump

The refrigerant pump (1) was a gear pump of the type MICROPUMP 219. By means of controlling the voltage (0 to 24 V) it was possible to vary the number of revolutions infinitely between 0 and 3,000 rpm. The maximum capacity of the pump was 2.5 l/min.

3.2.3 Coolant Pumps

The main pump (13) is a centrifugal pump of the type GRUNDFOS CHI 4-60 with a capacity of 10 l/min at 6 bar. It was driven by a 220 V AC motor.

During the Wilson Plot calibration and the experiments it was necessary to vary the coolant (water) flow rate in a wide range. In the high end of the range a large pressure drop had to be overcome. Therefore a 'booster' pump was needed (14). This pump was a centrifugal pump of the type GRUNDFOS CH 2-50 with a capacity of 10 l/min at 4 bar. It was connected in series to the main pump. This pump was only used when high coolant flow rates were required. The maximum coolant flow rate was about 12 l/min when both pumps were used.

3.2.4 Bypasses

To regulate the coolant flow rate and to discharge the heat delivered by the coolant pumps several bypasses were placed in the coolant loop. The main bypass was from the outlet of the booster pump (14) to the inlet of the coolant cooler (10). This was used to 'discharge' the heat delivered by the pumps to the coolant. While the pumps were running, the bypass could be controlled with a valve such that the temperature did not increase. To control the flow rate through the coolant loop, there was a valve at the outlet of the booster pump (14). To adjust the mass flow rate more precisely, two bypasses were placed around this valve. There was also a bypass around the coolant filter (15), because a huge pressure drop occurred over the filter in case of high flow rates. When a high flow rate was needed, this bypass could be opened.

3.3 Measurement Equipment

This section describes the instrumentation and measurement components used. During the tests it was necessary to measure temperatures, pressures, mass flow rates, and electrical power. All these data were logged and processed.

3.3.1 Temperature

Two different methods were used to measure the temperatures. Some temperatures were measured with thermocouples, and the more important temperatures (in the test section) were measured with Pt 100 sensors.

The thermocouples were of the type T, Copper (Cu) / Constantan (CuNi). The reference temperature was given by crushed ice. Pt 100 elements measured the temperatures required to

determine the heat transfer rate in the test section, i.e. the temperatures at the inlet and the outlet of the test section on the refrigerant side ($t_{ref,its}$, $t_{ref,ots}$) and on the coolant side ($t_{cool,its}$, $t_{cool,ots}$).

3.3.2 Pressure

The pressures $p_{ref,ips}$ and $p_{ref,its}$ were each measured with a pressure transducer of the type HONEYWELL STA3000 (gauge = pressure over atmospheric pressure. The atmospheric pressure of the laboratory was added to obtain absolute pressure). The refrigerant pressure difference between test section inlet at outlet (Δp_{ref}) was measured with a HONEYWELL STD924 transducer. Manometers were also connected to the coolant inlet and outlet to determine the pressure drop on the coolant side along the test section.

3.3.3 Mass Flow

Refrigerant mass flow rate was measured with a Coriolis-type DANFOSS MASS 2100 sensor connected to a DANFOSS MASS 3000 signal converter.

Coolant mass flow rate was also measured with a Coriolis-type mass flow meter, but the sensor was a RHEONIK RHM 04 GNT connected to a RHEONIK RHE 08 signal converter.

3.3.4 Electrical Power

The electrical power for the pre-heat section was regulated by means of two variable resistances and displayed on two ELCONTROL VIPD watt transducers. The logged signals, however, were supplied by two L-Unit LWT-24-A1-H watt transducers.

3.3.5 Data Logging and Processing

Data from thermocouples, pressure transducers, mass flow meters and watt transducers were processed and logged by a KEITHLEY 7001 Switch System and a KEITHLEY 2010 Multimeter. The switcher changed between the different input channels, while the multimeter measured the voltage, digitised it, and sent it to a PC.

The KEITHLEY data logger was not capable of measuring with Pt 100-elements. Therefore an AΣΑ F250 MK II Precision Thermometer was used combined with an AΣΑ SB250 Multichannel switch box.

The PC processed the data by a computer program developed at SINTEF Energy Research. It converted the data to values with physical units. The data could also be shown as graphs on the computer screen. At the same time the program wrote them to a file which could be processed by other programs.

After the measurement, these data files could be analysed in MS EXCEL97 worksheets. The thermodynamic and transport properties of the refrigerant and of the coolant were supplied by the libraries xlco2lib.dll and h2oprop_p.xls, respectively, which were also developed at SINTEF Energy Research.

`xlco2lib.dll` is an implementation of the IUPAC thermodynamic equations [42] with improvements [43], as well as transport properties [44].

4 WILSON PLOT CALIBRATION

As mentioned in Chapter 2, it is necessary to have knowledge of the heat transfer coefficient on the 'coolant' (water) side (α_c) to determine the heat transfer coefficient of the refrigerant (α_h) by means of the heat transfer rate (\dot{Q}) and the overall heat transfer coefficient (k) in a heat exchanger. On beforehand, α_c was unknown. Common correlations for turbulent single-phase flow could not be used, due to the geometry of the test section and the desired accuracy of the data. A correlation for the water-side heat transfer coefficient α_c was found using a modified Wilson plot method.

A short description of the principles can be found in Section 4.1. The results are presented in Section 4.2.

4.1 Principles of the Wilson Plot Method

The Wilson plot method was introduced in 1915 by E.E. Wilson as a tool for designing shell-and-tube condensers and feed water heaters [23]. In this work, the Wilson plot method is modified as described in [25].

The Dittus-Boelter-type equation is a well-known expression for the single-phase heat transfer coefficient in a turbulent flow:

$$\alpha_c = C \cdot Re^m \cdot Pr^n \cdot \frac{\lambda}{d_{hyd}} \quad (24)$$

This equation is used to describe the heat transfer coefficient on the water-side. For this purpose, the Reynolds number exponent (m) and the constant (C) are assumed to be unknown, but they can be found with the Wilson Plot technique. The Prandtl number exponent (n) is commonly taken to be as $n = 0.4$ for heating and $n = 1/3$ for cooling [14].

Combining the equation for the overall heat transfer coefficient (7) with equation (24) yields

$$\left(\frac{1}{k} - R_w \right) \cdot \frac{A_c}{A_h} = \frac{1}{C} \cdot \frac{1}{\left(Re^m \cdot Pr^n \cdot \frac{\lambda}{d_{hyd}} \right)_c} + \frac{A_h}{\alpha_h \cdot A_c} \quad (25)$$

This is an equation on the form

$$Y_1 = A \cdot X_1 + B \quad (26)$$

where the slope A equals

$$A = \frac{1}{C}, \quad (27)$$

the independent variable is

$$X_1 = \frac{1}{\left(\text{Re}^m \cdot \text{Pr}^n \cdot \frac{\lambda}{d_{hyd}} \right)_c} \quad (28)$$

and the intersection with the y -axis (B) equals

$$B = \frac{A_h}{\alpha_h \cdot A_c}. \quad (29)$$

The dependent variable (Y_1) is defined as

$$Y_1 = \left(\frac{1}{k} - R_w \right) \cdot \frac{A_c}{A_h} \quad (30)$$

In Equation (30), the overall heat transfer coefficient (k) is known from the experiment, since the transferred heat, the heat transferring area and the mean temperature difference is given by the measurements and the geometry. The wall resistance R_w may be calculated (or neglected) and A_c , A_h , and d_{hyd} are geometry data. Thus Y_1 is known.

The Reynolds number (Re) and the Prandtl number (Pr) as well as the thermal conductivity (λ) are known from the coolant properties. Since m is not known in Equation (28), X_1 is unknown. During the experiments, the independent variable X_1 can be varied by changing the mass flow of the coolant (\dot{M}_c). This corresponds to a variation of the Reynolds number. In all experiments, the coefficient B has to be constant, i.e. α_h has to be constant during the plot. Therefore, the following conditions are required:

- The mass flow \dot{M}_h had to be constant.
- The hot side mean temperature \bar{t}_h and the inlet and outlet temperatures ($t_{ref,its}$ and $t_{ref,ots}$) had to be constant (constant heat transfer rate \dot{Q}).
- In order to keep \dot{Q} constant while varying \dot{M}_c , the coolant inlet and outlet temperature, i.e. ΔT_c , and the mean temperature (\bar{t}_c) had to be varied.

With the experimental results, a plot of Equation (25) can be made. Figure 9 shows such a plot.

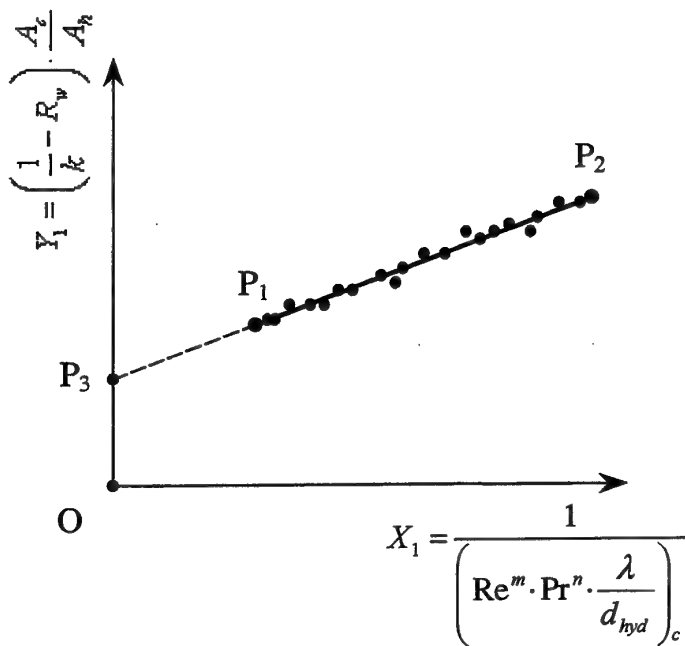


Figure 9: A Wilson Plot

The line $\overline{P_1P_2}$ is a linear curve fit to the measured data. If it is assumed that the heat transfer coefficient on the coolant side becomes infinitely high for an infinite coolant mass flow (\dot{M}_c), the line may be extrapolated to the y -axis. The intersection is indicated with point P_3 . This point corresponds to an infinite Reynolds number (Re_c) and therefore to an infinite coolant mass flow rate, thus X_1 becomes zero (see Equation(28)). The length $\overline{OP_3}$ then represents the thermal resistance on the inner side of the tube (B).

Solution Algorithm

In Equation (25) there are three unknowns: α_h , C , and m . Unfortunately it is not possible to solve a linear plot with more than two unknowns. Therefore a solution algorithm must be found (curve fit). As can be seen in Figure 11, this algorithm consists mainly of two steps. First a value of m has to be guessed, and then the plot can be made. With a second plot, the so-called logarithmic Wilson Plot (Figure 10), the 'goal seek' for m can be checked:

Equation (25) can be written as

$$\left(\frac{1}{k} - R_w - \frac{1}{\alpha_h} \right) \cdot \frac{A_c}{A_h} \cdot \left(Pr^n \cdot \frac{\lambda}{d_{hyd}} \right)_c = \frac{1}{C \cdot Re_c^m} \quad (31)$$

or

$$y_2 = \frac{1}{C \cdot Re_c^m} \quad (32)$$

Taking the logarithm of (32) results in

$$\ln y_2 = \ln \left(\frac{1}{C \cdot Re_c^m} \right) \quad (33)$$

or

$$\ln y_2 = -m \cdot \ln (Re) - \ln C \quad (34)$$

This equals also to a linear equation of the form

$$Y_2 = D \cdot X_2 + E. \quad (35)$$

where the slope D is defined with

$$D = -m \quad (36)$$

and the independent variable X_2 is defined as

$$X_2 = \ln (Re) \quad (37)$$

as well as the intersection with the y -axis (E) equals

$$E = -\ln C. \quad (38)$$

By re-substituting y_2 we get the dependent variable Y_2 as

$$Y_2 = \ln \left\{ \left(\frac{1}{k} - R_w - \frac{1}{\alpha_h} \right) \cdot \frac{A_c}{A_h} \cdot \left(Pr^n \cdot \frac{\lambda}{d_{hyd}} \right) \right\}. \quad (39)$$

If the m from equation (36) and the initially guessed m are the same, then the solution for m is found. If not, a more qualified Reynolds exponent m has to be guessed. In MICROSOFT EXCEL97 this can easily be done by using the SOLVER function. With this algorithm, one can find the constant (C) and the Reynolds number exponent (m) needed for the Dittus-Boelter-type equation (24). See Figure 11.

It was assumed that this equation described the heat transfer coefficient on the outer side of the tube as long as the flow was turbulent.

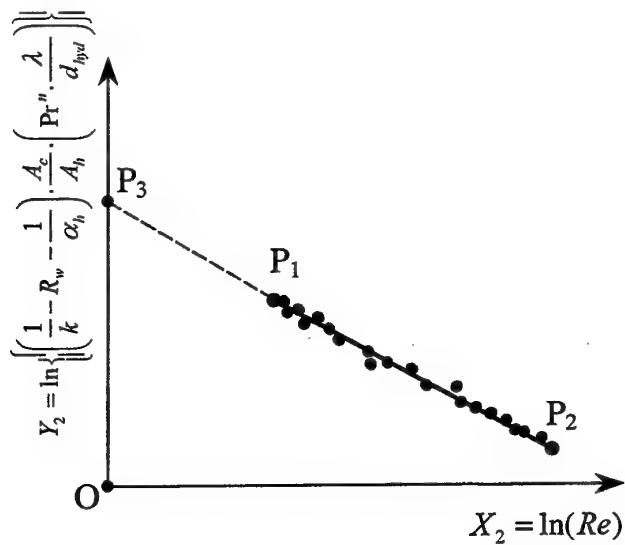


Figure 10: A logarithmic Wilson Plot

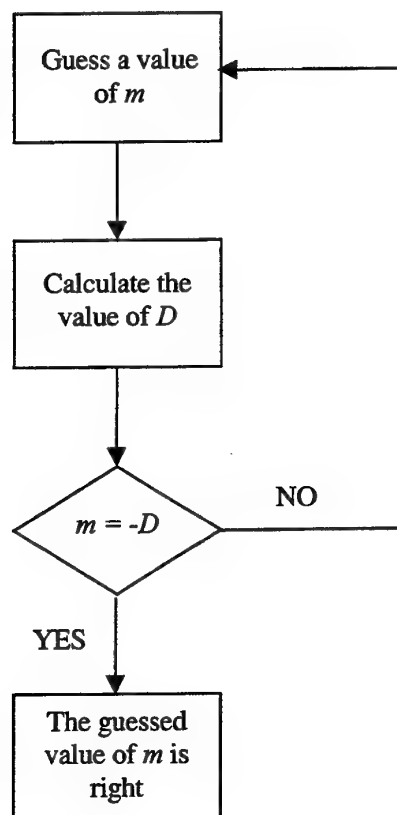


Figure 11: Flow chart diagram of the Wilson Plot algorithm

4.2 Results of the Wilson Plot

4.2.1 Water Heating

During this Wilson Plot, the refrigerant was supercritical with a pressure of $p_{CO_2} = (91 \pm 0.9)$ bar and an inlet temperature of $t_{CO_2,its} = (30 \pm 0.2)^\circ\text{C}$. The heat flux was kept constant at $\dot{q} = (20 \pm 0.65) \text{ kW/m}^2$. Since the accuracy of the calibration is improved with a higher heat transfer coefficient on the refrigerant-side (α_h), a mass flux of $\dot{m}_{CO_2} = (2000 \pm 42) \text{ kg/(m}^2\cdot\text{s)}$ was chosen. These data corresponded to a temperature drop of $\Delta T_{CO_2} = (7.7 \pm 0.2) \text{ K}$ in the test section.

The mean temperature in the test section, $\bar{t}_{CO_2} = (25.7 \pm 0.4)^\circ\text{C}$, was close to the room temperature in the laboratory; therefore the heat loss to the ambient was minimal.

The measurements were made when the desired values were reached and the rig was operating in steady-state conditions. All data were logged and written to a file by the PC. For each measured point, about 20 readings were taken with a time interval of 60 seconds. The calibration was made with a total of 29 different water mass flow rates ($\dot{M}_{H_2O} = 2 \text{ to } 9.8 \text{ kg/min}$).

By means of the Wilson plot technique, the graphs shown in Figure 12 and Figure 13 were found. The plot gave

$$C = 0.202 \quad \text{and} \quad m = 0.607. \quad (40)$$

and the 'calibrated' equation for the water side heat transfer coefficient (α_c) during heating mode had the form

$$\alpha_{c,heat} = 0.202 \cdot Re^{0.607} \cdot Pr^{0.4} \cdot \lambda / d_{hyd}. \quad (41)$$

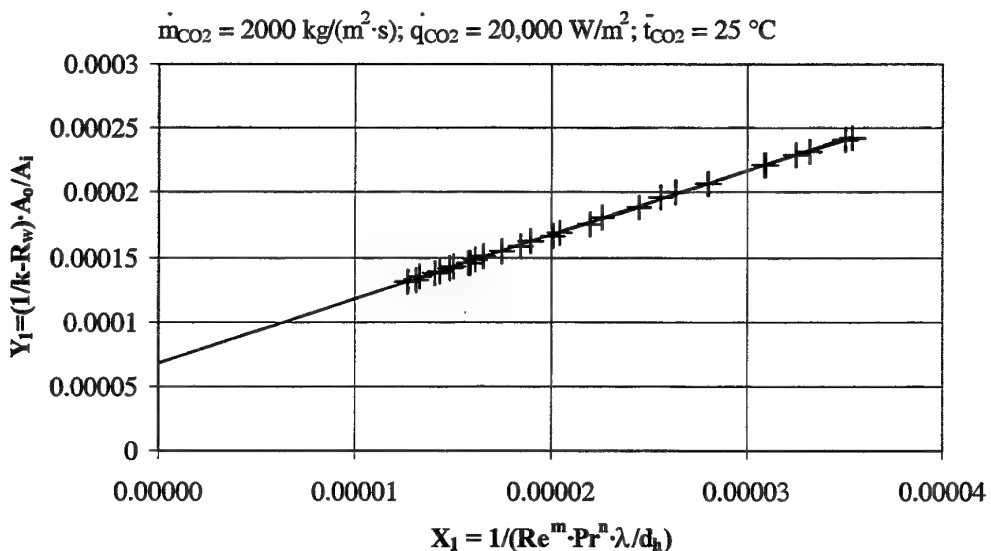


Figure 12: Wilson plot for water heating ($C = 0.202$ and $m = 0.607$)

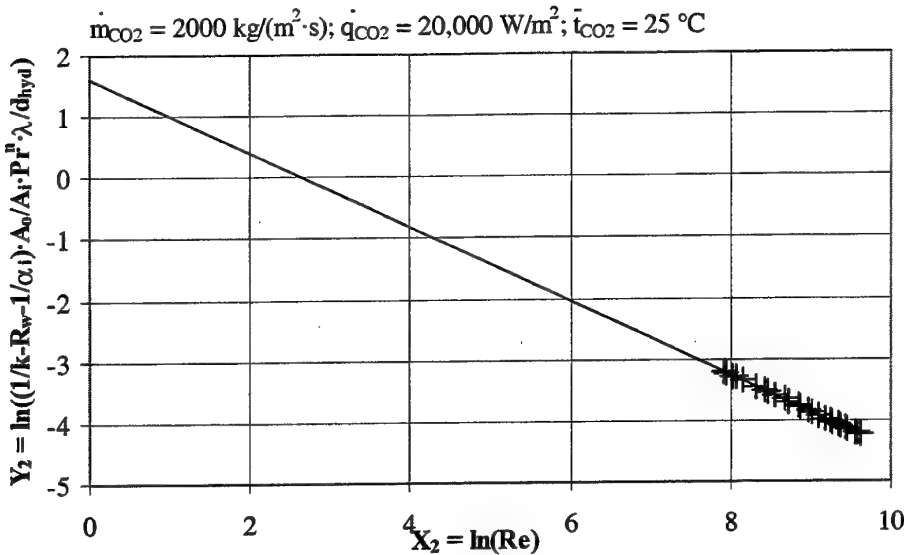


Figure 13: Logarithmic Wilson plot for water heating ($C = 0.202$ and $m = 0.607$)

As described in Section 4.1, C is the inverse of the slope of the fitted curve (straight line) in Figure 12 and m is the negative of the slope of the fitted curve (straight line) of Figure 13.

4.2.2 Water Cooling

It was decided to perform a second Wilson plot calibration for the evaporation tests when the water was cooled by the CO_2 . For this calibration, the test conditions on the inside of the tube (refrigerant side) again had to be constant. The CO_2 pressure was set to $p_{CO_2} = (91 \pm 0.7)$ bar and the test section inlet temperature was constant at $t_{CO_2,ins} = (4.7 \pm 0.1)^\circ\text{C}$. With a heat flux of $\dot{q} = (20 \pm 0.38) \text{ kW/m}^2$ and a specific mass flux of $\dot{m}_{CO_2} = (2000 \pm 14) \text{ kg/(m}^2\cdot\text{s)}$, the resulting temperature rise and the mean refrigerant temperature was $\Delta T_{CO_2} = (10.6 \pm 0.2) \text{ K}$ and $\bar{t}_{CO_2} = (11.3 \pm 0.5)^\circ\text{C}$, respectively. Experiments at a total of 20 different water mass flow rates were carried out ($\dot{M}_{H_2O} = 1.7$ to 9.4 kg/min).

The graphs of the Wilson Plot are shown in Figure 14 and Figure 15, and the resulting Wilson Plot constants were

$$C = 0.162 \quad \text{and} \quad m = 0.653 \quad (42)$$

The resulting equation for the water heat transfer coefficient in cooling mode was

$$\alpha_{c,cool} = 0.162 \cdot Re^{0.653} \cdot Pr^{1/3} \cdot \lambda / d_{hyd}. \quad (43)$$

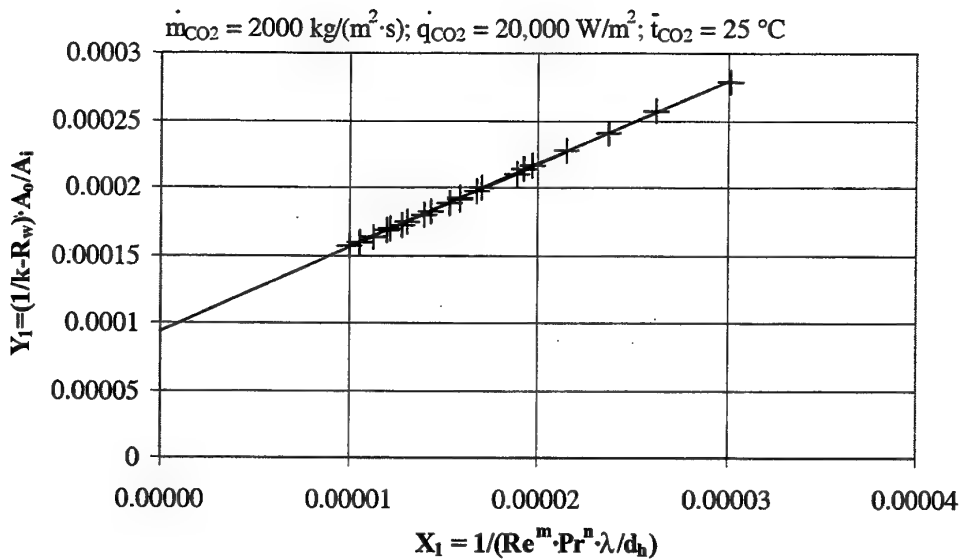


Figure 14: Wilson Plot for water cooling ($C = 0.162$ and $m = 0.653$)

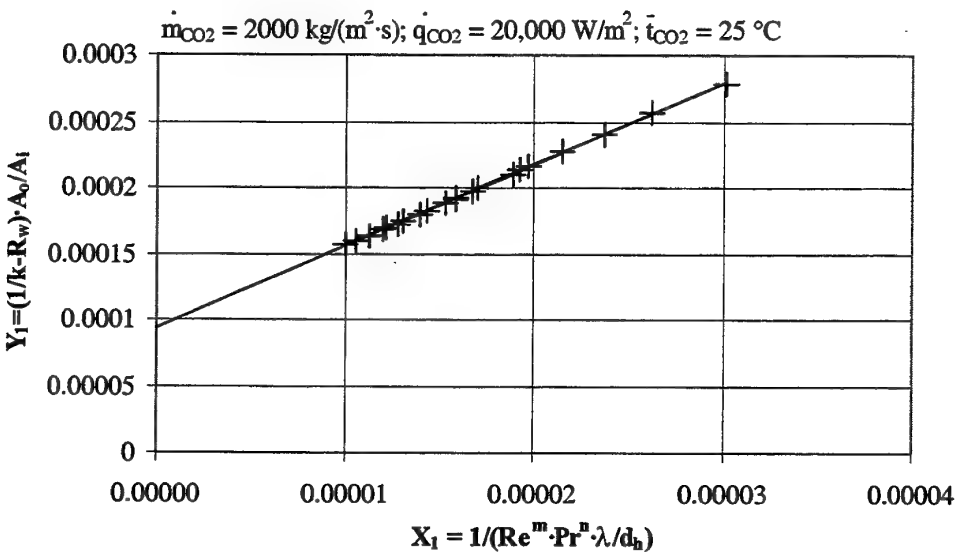


Figure 15: Logarithmic Wilson Plot for water cooling ($C = 0.162$ and $m = 0.653$)

4.2.3 Comparison of the Wilson Plots

The heating and cooling Wilson plots did not show the same result, i.e. two different equations were yielded. Figure 16 shows the calculated heat transfer coefficient according to the equations (41) and (43) at a temperature of 20°C depending on the mass flow rate.

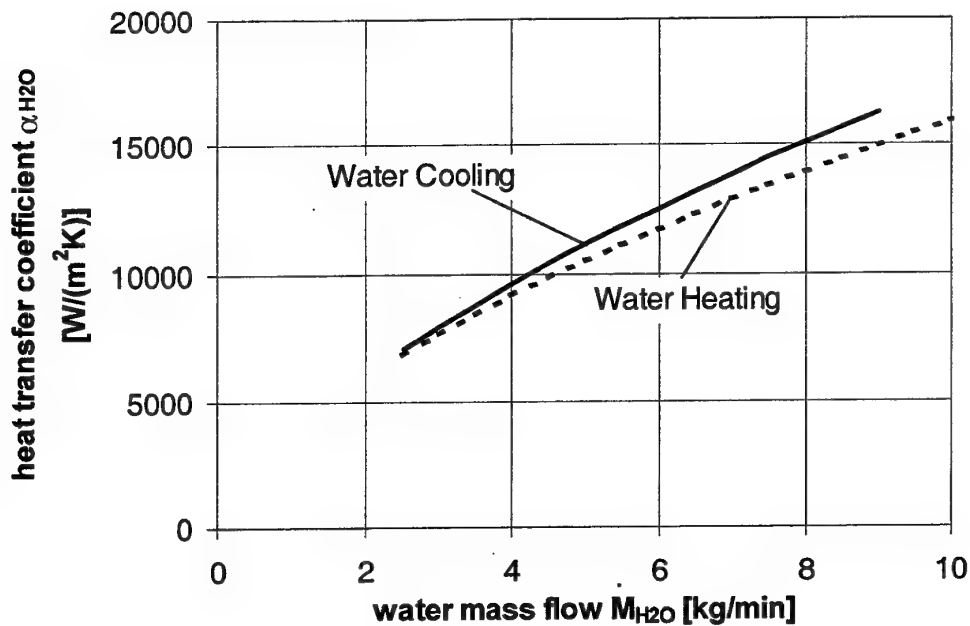


Figure 16: Heat transfer coefficient of water

As can be seen, the heat transfer coefficient is slightly higher for water cooling (evaporation tests see Chapter 5.1) than for water heating (gas cooling tests see Chapter 5.2). However, most of the experiments were carried out at water flow rates between $\dot{M}_{H2O} = 3$ to 5 kg/min, where the deviation between the two curves is quite small.

5 RESULTS

This chapter describes the experimental results for the heat transfer coefficient and pressure drop at

- Super-critical (cooling), and
- Sub-critical conditions (evaporation).

After a brief description of the test conditions, the measured values are compared with 'common' correlations from the literature. Since the heat exchanger used has a certain length, mean values rather than local values were determined. The exact procedure is described in Chapter 2.

For the comparisons to calculation models, the 'local' values with respect to the mean properties along the test section were used. The heat transfer and pressure drop data are compared in a quantitative and qualitative way. The quantitative comparisons were done by means of the average deviation (σ_{avg}) and the mean deviation (σ_{mean}):

$$\sigma_{avg} = \frac{1}{n} \sum_n \frac{(\alpha_{calc} - \alpha_{meas})}{\alpha_{meas}} \quad (44)$$

$$\sigma_{mean} = \frac{1}{n} \sum_n \left| \frac{(\alpha_{calc} - \alpha_{meas})}{\alpha_{meas}} \right|, \quad (45)$$

where n is the total number of measurements, α_{calc} is the calculated local and α_{meas} is the measured mean heat transfer coefficient. For the pressure drop, the analogous deviations were used.

5.1 Supercritical Conditions (Cooling)

5.1.1 General

Figure 17 shows a schematic diagram of a cooling 'test point'. (See Figure 3 and Figure 4 for the flow chart of the test rig.)

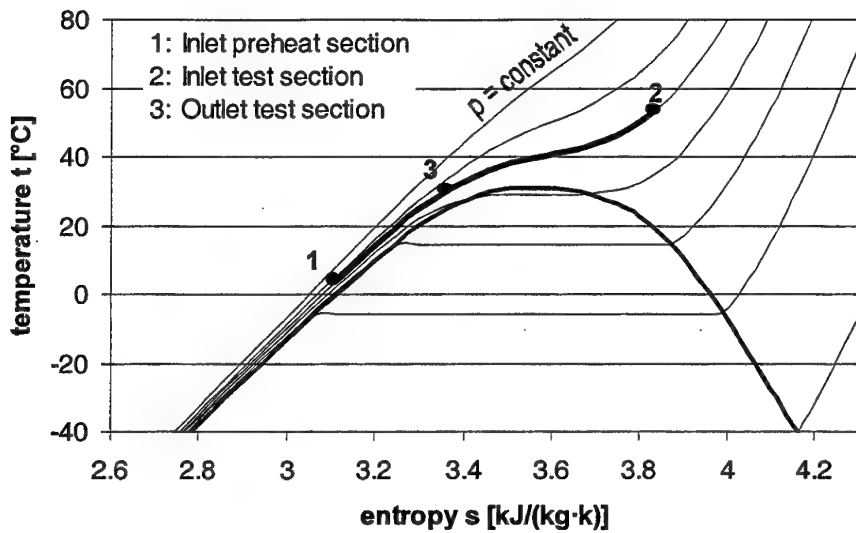


Figure 17: Schematic temperature-entropy diagram of a gas cooling process

Refrigerant entered the preheat section at a super-critical pressure and a sub-critical temperature (1). Then heat was added electrically in the preheat section before the CO₂ entered the test section (2). The heat transfer to the water circuit took place in the test section. The cooled CO₂ exited the test section (3) and was cooled down in the CO₂ cooler before it reached the refrigerant pump inlet (1).

In order to allow an analysis of the heat transfer and pressure drop characteristic, a total of six test series were carried out. The tests were done at different mass flow rates (mass fluxes, \dot{m}), pressures (p) and heat fluxes (q). Table 1 summarises the test conditions.

Table 1: Overview of the cooling test conditions

q (kW/m ²)	p (bar)			
		81	91	101
20	600	-	Gas cooling No. 6	-
	900	Gas cooling No. 4	Gas cooling No. 3	Gas cooling No. 5
	1200	-	Gas cooling No. 2	-
10	600	-	Gas cooling No. 1	-

Table 2 shows the test conditions and the experimental tolerances of the points. As can be seen, the mass flux was kept within a range of about $\pm 2\%$ and the pressure showed a tolerance of $\pm 1\%$.

Table 2: Test conditions and experimental tolerances

Test	q (kW/m^2)	m ($\text{kg}/(\text{m}^2 \cdot \text{s})$)	p (bar)
Gas cooling No. 1	$10^{+1.0}_{-1.4}$	600 ± 11	91 ± 0.96
Gas cooling No. 2	$20^{+0.9}_{-1.7}$	1200 ± 16	91 ± 0.87
Gas cooling No. 3	$20^{+1.5}_{-0.6}$	900 ± 13	91 ± 0.59
Gas cooling No. 4	$20^{+5.2}_{-3.7}$	900 ± 19	81 ± 0.30
Gas cooling No. 5	$20^{+0.6}_{-0.6}$	900 ± 6	101 ± 0.36
Gas cooling No. 6	$20^{+1.4}_{-1.0}$	600 ± 12	91 ± 0.44

Only the heat flux showed a wider range, but this is of secondary importance, as also shown by the results (see below).

Each of the series consisted of about five points at different mean temperatures (\bar{t}). One point was always close to the pseudo-critical temperature (maximum c_p) and at least two were above and two below this important temperature. The pseudo-critical temperatures and the corresponding maximum specific isobaric heat capacities at the relevant pressures are given in Table 3.

The choice of test points below and above the pseudo-critical temperature was done such that the enthalpy differences between the points were approximately constant. However, some series were influenced by constraints given by the test rig. In order to set the inlet temperature to the desired value, the refrigerant was heated electrically in the preheat section, but the capacity was limited at $P_{el} = 3 \text{ kW}$. This effected for example the test 'Gas cooling No. 2' with $\dot{m} = 1200 \text{ kg}/(\text{m}^2 \cdot \text{s})$, where the maximum capacity of the preheat section was reached at a rather low inlet temperature of about 48°C .

Table 3: Pseudo-critical temperature and maximum specific heat capacity

p (bar)	t_{pseudo} ($^\circ\text{C}$)	c_p ($\text{kJ}/(\text{kg} \cdot \text{K})$)
81	35.2	29.4
91	40.6	12.0
101	45.6	7.8

The temperature drop along the test section is given by the mass flow rate, i.e. by the mass flux and the cross section, and the heat flux (\dot{q}) that is based on the perimeter of the ports.

5.1.2 Heat transfer at super-critical pressures

In this section, the measured single-phase heat transfer coefficients are compared with calculation models. The following models are used:

- Different forms of Gnielinski's correlation:
 - simple Gnielinski: Gnielinski's correlation for the Nusselt number using the Haaland friction factor [21] but neglecting the influence of the wall temperature (Roughness $\epsilon = 1.0 \cdot 10^{-6}$ m).
 - Gnielinski: Gnielinski's correlation using the Haaland friction factor and considering the influence of the wall temperature,
 - Gnielinski (VDI): Gnielinski's correlation using the Filonenko friction factor (according to [28]).
- The 'special' models developed for heat transfer at super-critical pressures:
 - Polyakov [29]
 - Ghajar & Asadi [30]²
- And the Dittus-Boelter correlation [14] with different Prandtl exponents (n) (compare equation (24) with $C = 0.023$, $m = 0.8$):
 - $n = 1/3$: which is the 'correct' value for a flow under cooling mode
 - $n = 0.4$: which is normally used for heating mode.

The comparison of the experimental data with these models showed a quite good correspondence. Table 4 contains the average and the mean deviations of the 32 points measured and Figure 18 to Figure 20 visualise the good correspondence graphically.

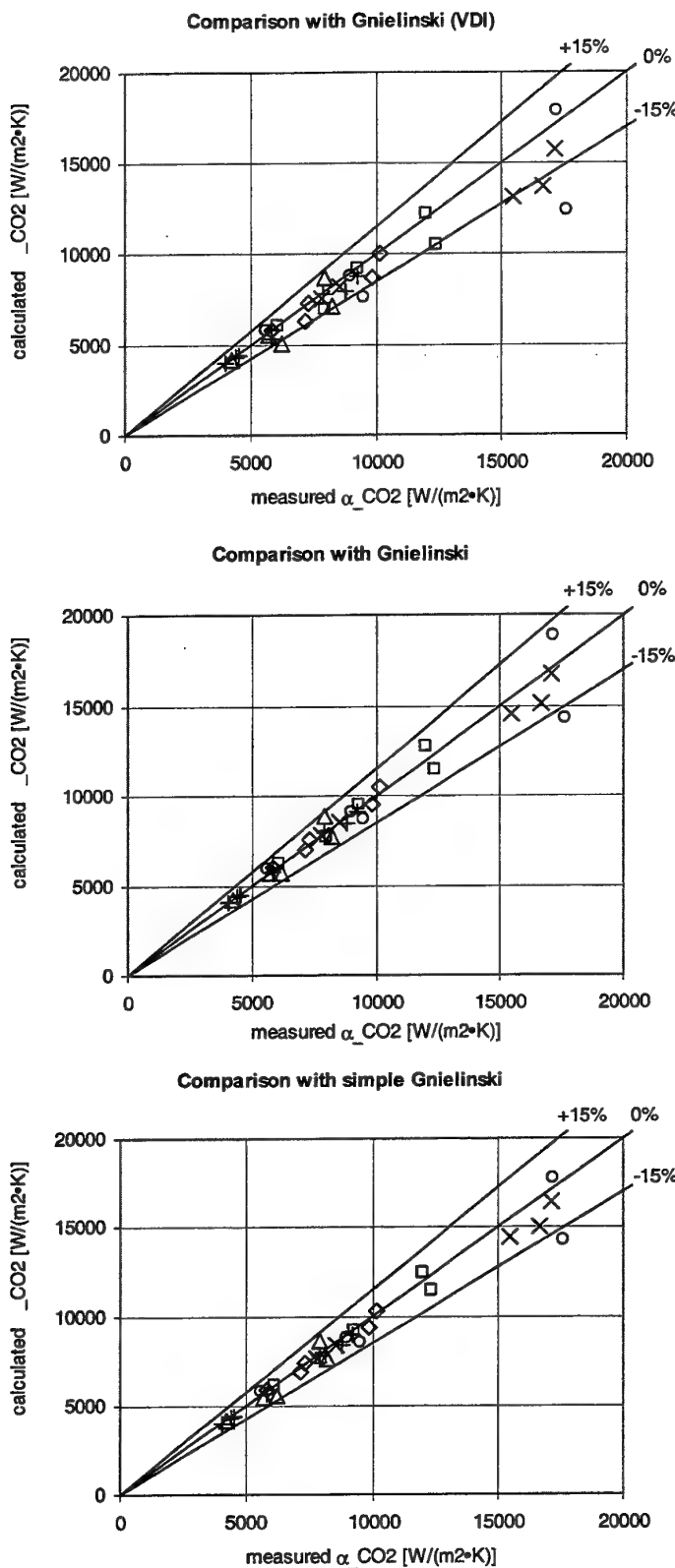
Table 4: Deviation of the measured heat transfer to calculation models

	References	σ_{avg} [%]	σ_{mean} [%]
simple Gnielinski	see above	-3	4
Gnielinski	see above	-1	4
Gnielinski (VDI)	[28]	-7	8
Polyakov	[29]	19	19
Ghajar & Asadi	[30]	1	8
Dittus-Boelter ($n = 1/3$)	[14]	-18	18
Dittus-Boelter ($n = 0.4$)	see above	-7	9

Gnielinski's model in combination with Haaland's friction factor as well as the model proposed by Ghajar & Asadi predict very well the super-critical heat transfer coefficient of CO₂ under cooling mode in the temperature region investigated. A mean deviation of only 4% was calculated for Gnielinski's model.

The fit of the rather complicated model proposed by Polyakov was worse than the values according to the standard Dittus-Boelter correlation. However, the fit of the Dittus-Boelter correlation using a Prandtl exponent of $n = 0.4$ ($\sigma_{mean} = 9\%$) was much better than when using $n = 1/3$ ($\sigma_{mean} = 18\%$).

² The Ghajar and Asadi correlation comes with its own equation of state. This has not been implemented here. The IUPAC equations [42,43] have been used as for all calculations. It might be that the Ghajar and Asadi correlation would have fit better to the test data if its "own" equation of state had been used.



+ p90 m600 q10 × p90 m1200 q20 □ p90 m900 q20 Op80 m900 q20 ◇ p9100 m900 q20 △ p90 m600 q20

Figure 18: Comparison of measured heat transfer coefficients with calculation models

As one can see from Figure 18, most of the calculated values fitted the experimental data within a deviation of $\pm 15\%$. Only the Polyakov correlation overestimated the heat transfer coefficient (Figure 19) while the Dittus-Boelter correlation underestimated it (Figure 20).

The following subsections briefly describe the qualitative dependence of the heat transfer coefficient on the temperature and analyse the influence of heat flux, mass flow rate, and pressure. Figure 21 to Figure 23 show a comparison of the measured values with Gnielinski's correlation (curves). In the figures, the mean temperatures of each experiment is indicated with markers while the bars indicate the "overall cooling processes" (inlet temperature to outlet temperature).

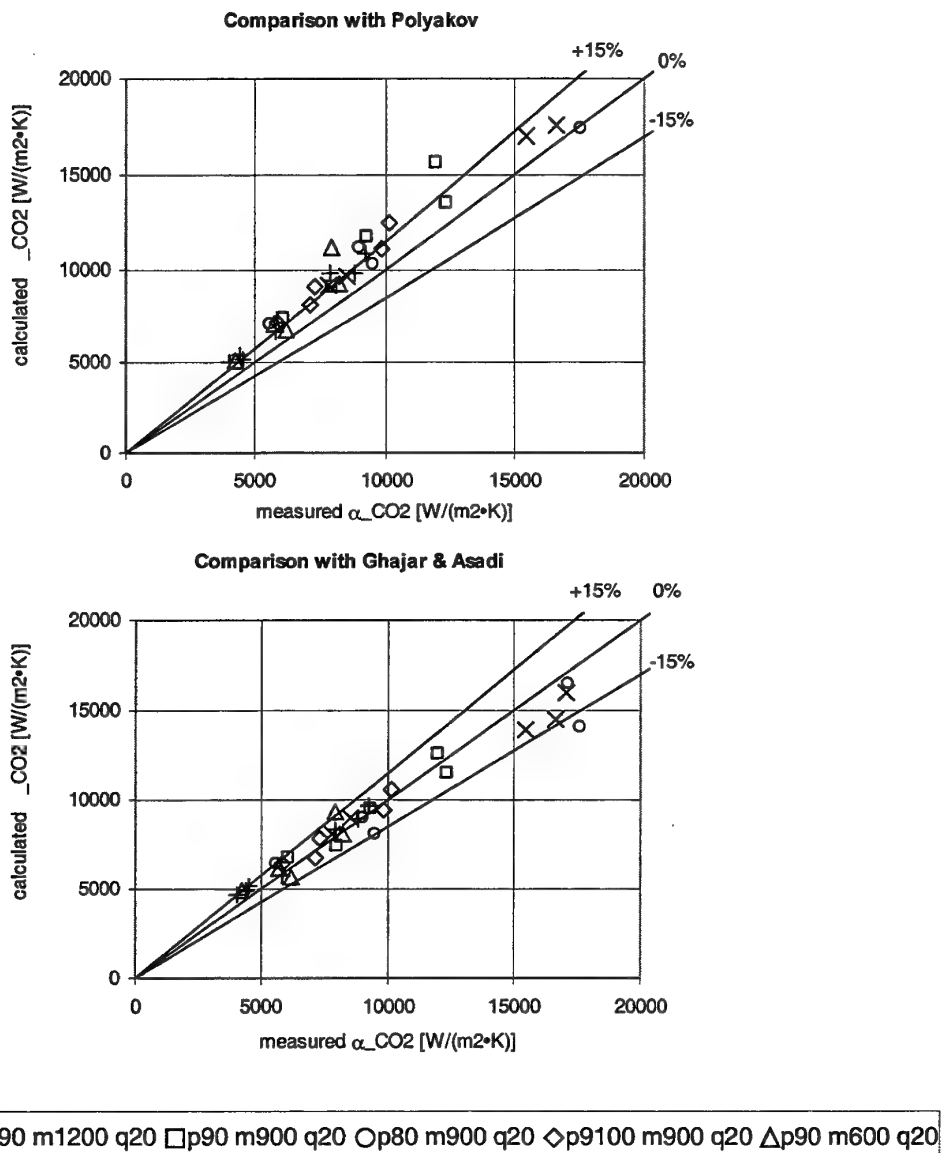
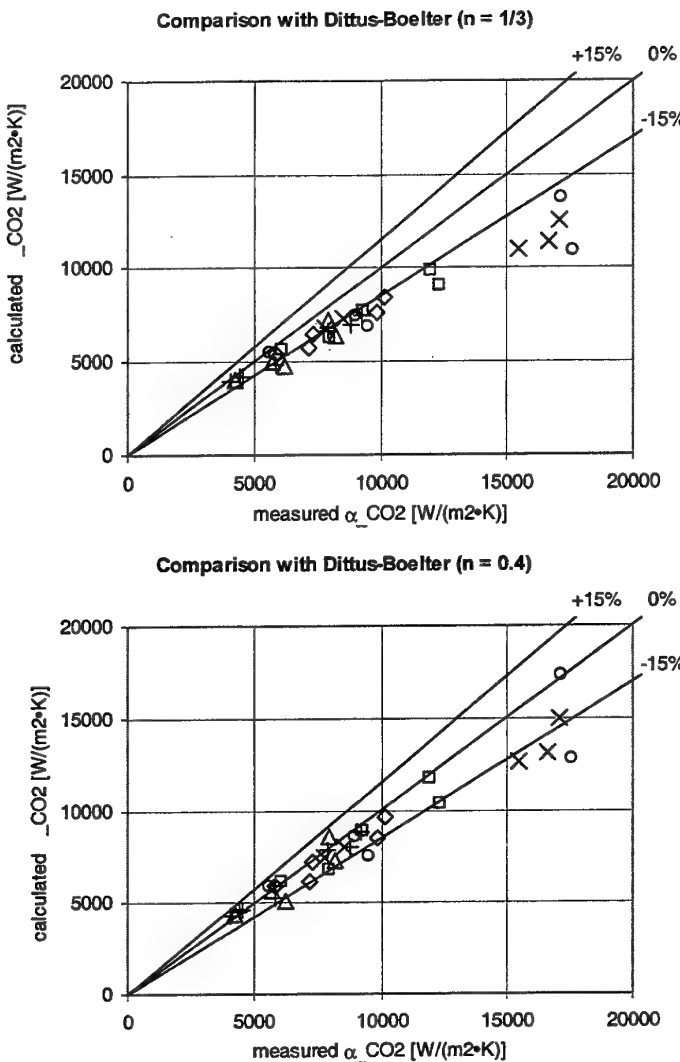


Figure 19: Comparison of measured heat transfer coefficients with calculation models



+ p90 m600 q10 × p90 m1200 q20 □ p90 m900 q20 Op80 m900 q20 ◇ p9100 m900 q20 Δ p90 m600 q20

Figure 20: Comparison of measured heat transfer coefficients with calculation models

Influence of heat flux:

The influence of the heat flux on the heat transfer coefficient was rather small, as can be seen from Figure 21. Gnielinski's correlation for the Nusselt number takes into account the heat flux by means of the factor $(Pr/Pr_w)^{0.11}$. Since the wall temperature changes with heat flux, the Prandtl number at wall temperature Pr_w changes as well. However, due to the small exponent of 0.11, the correction factor does not vary much.

If the heat flux rises, the heat transfer coefficient makes an almost parallel translation to lower temperatures. This means that below the pseudo-critical temperature - indicated with the peak of the heat transfer coefficient - the heat transfer coefficient rises slightly, and above it becomes slightly lower in case of a higher heat flux. A closer investigation showed that if the heat flux is increased from 10,000 to 20,000 W/m^2 the (calculated) variation of the heat transfer coefficient corresponds to an average change of 1.4% in the temperature region from 10 to 80°C.

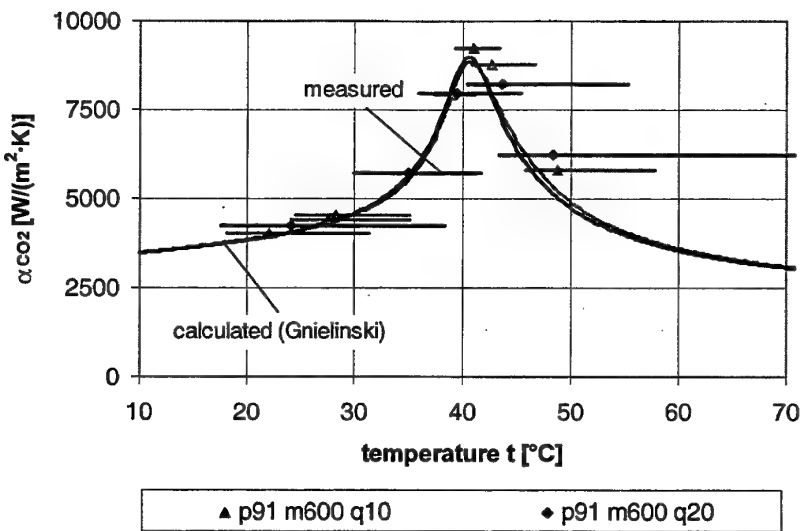


Figure 21: Influence of the heat flux on the heat transfer coefficient

The comparison of measurement and calculation showed a high accuracy for both series.

Influence of mass flow rate:

In contrast to that of the heat flux, the influence of the mass flow rate was significant. A higher mass flow rate of course lead to a higher heat transfer coefficient. This can be seen from Figure 22. The calculations showed that the average heat transfer coefficient rose by about 42% if the mass flux was increased from 600 to 900 kg/(m²·s), and by 82% if the mass flow was increased to 1200 kg/(m²·s).

The agreement between calculation and measurement was quite satisfactory (Figure 22). Only at high temperatures could a moderate deviation be seen.

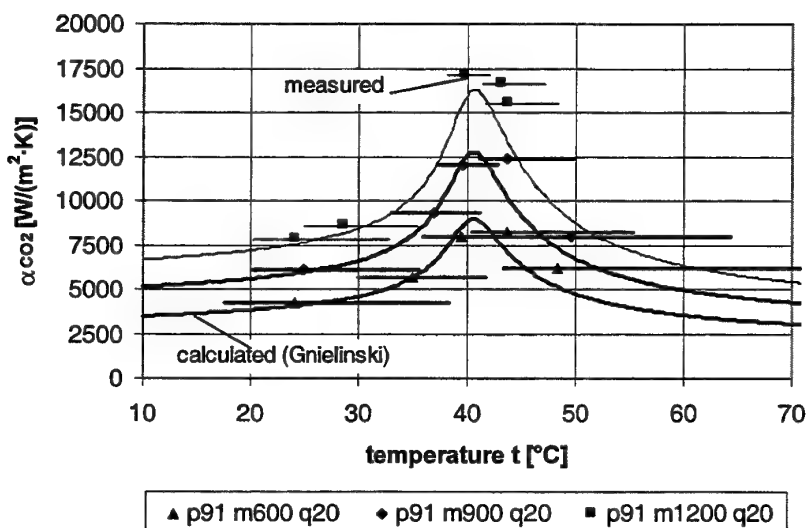


Figure 22: Influence of the mass flow on the heat transfer coefficient

Influence of pressure:

The change of the pseudo-critical temperature with pressure is of special interest (Table 3). Since the heat transfer coefficient reaches a maximum at the pseudo-critical temperature, this maximum will change with varying pressure.

Figure 23 shows this fact. The maximum heat transfer increases the closer the pressure comes to the critical pressure of the refrigerant ($p_{critical} = 73.83$ bar). At 81 bar the maximum value is higher than 21,000 W/(m²·K) and at 101 bar the maximum is about 10,000 W/(m²·K) at the pseudo-critical temperature. This corresponds to a rise of about 68% if the pressure decreases from 91 to 81 bar. If the pressure rises from 91 to 101 bar, the maximum heat transfer coefficient decreases by about 21%. At very low and very high temperatures, i.e. away from the pseudo-critical temperature, the influence of pressure is small. This can be seen by the asymptotic behaviour of the curves below about 25°C and above 80°C.

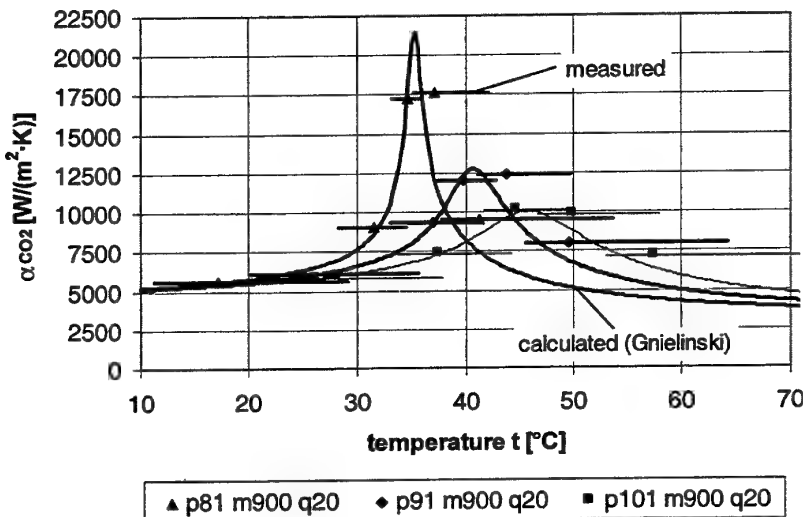


Figure 23: Influence of the pressure on the heat transfer coefficient

Again, the deviation between measurement and calculation was small.

5.1.3 Pressure drop at super-critical pressures

Similarly to what was done in the previous subsection, here the measured pressure drop data were compared with calculation models for the frictional pressure drop³. The selected models are:

- Blasius [28]: This is the common correlation for estimating the pressure drop in a smooth tube and turbulent flow.
- Colebrook & White [28]: This implicit form for the friction factor gives values in accordance to the well known Moody-Diagram. It can be applied in the transition region between non-turbulent and turbulent flow.

³ The pressure change due to deceleration is neglected here, because calculations have shown that this is low compared to the frictional pressure drop.

- Swamee et al. have published an explicit form of the Colebrook & White friction factor [31].

(Remark: For the latter two, the tube roughness was assumed to be $1 \cdot 10^{-6}$ m.)

The deviations of the calculated values from the measured data are shown in Table 5. As can be seen, the models predicted the pressure drop quite accurately. The mean deviation was approximately 2% for both the Colebrook & White and the Swamee model.⁴

Table 5: Deviation of the measured pressure drop to calculation models

References	σ_{avg} (%)	σ_{mean} (%)
Blasius [28]	-6	6
Colebrook & White [28]	1	2
Swamee [31]	1	2

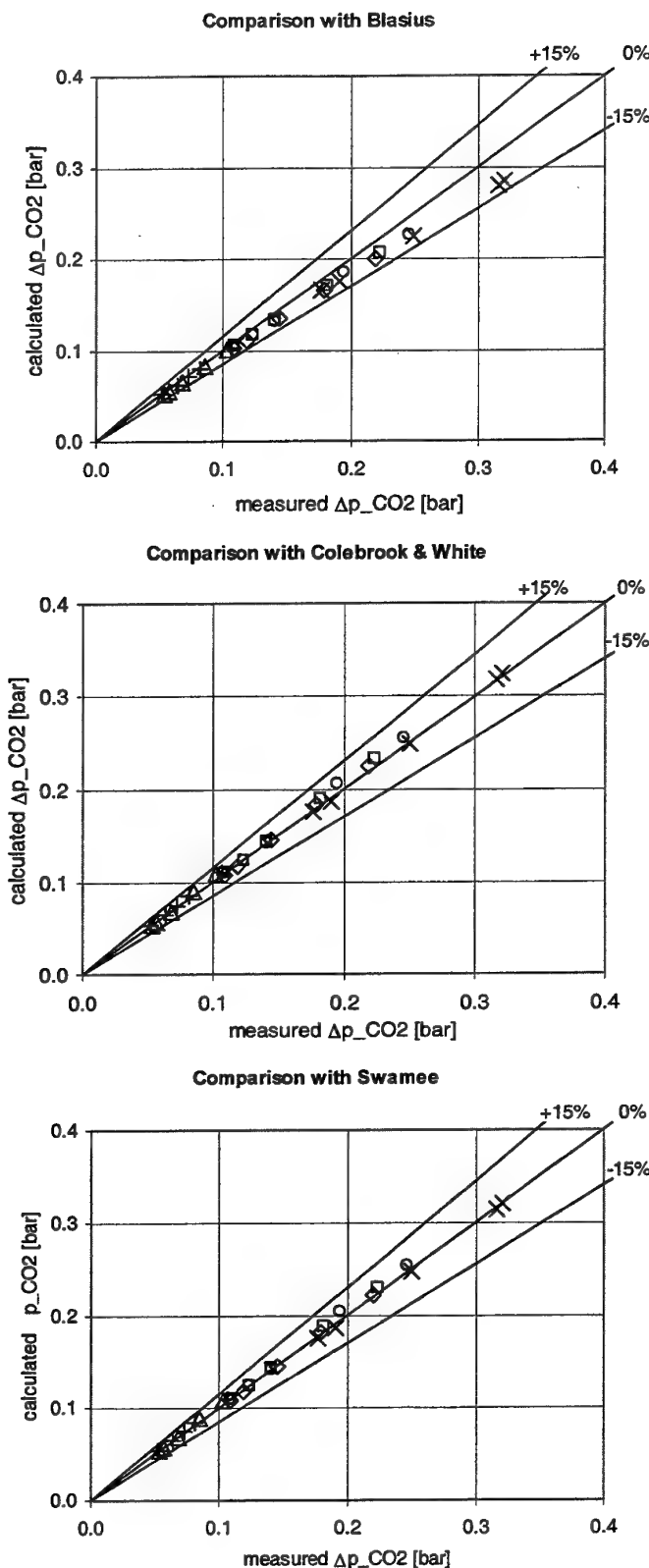
Only the Blasius correlation slightly underestimated the pressure drop. But this could be expected, because the present MPE tube made of aluminium had a certain roughness.

Figure 24 visualises the good fit of the models to the experiments. Almost every measured point is located on the line representing a deviation of 0%. Figure 25 to Figure 27 show the influence of heat flux, mass flow rate, and absolute pressure on the pressure drop.

As can be seen from Figure 25, there was no noticeable influence on the pressure drop of the heat flux. In contrary to that, the mass flow rate had a considerable effect (Figure 26). As stated above, the heat transfer coefficient rose by about 42% if the mass flow was changed from 600 to 900 $\text{kg}/(\text{m}^2 \cdot \text{s})$ and by about 82% if it was increased to 1200 $\text{kg}/(\text{m}^2 \cdot \text{s})$. However, at the same time the pressure drop rose about 100% and 240%, respectively.

In general, the dependence of the pressure drop on the temperature showed a change near the pseudo-critical temperature. The steep gradient near this temperature is caused by the rapid change of the density. Since the pressure has a large influence on the pseudo-critical temperature, the characteristic of the pressure drop changes with the absolute value of the pressure (Figure 27). In the temperature region from 10 to 80°C, the mean pressure drop increased about 17% if the pressure was changed from 91 to 81 bar and decreased 13% if the pressure rose from 91 to 101 bar. For the heat transfer coefficient the corresponding changes were 68 and 21%, respectively.

⁴ It should be noted that the Swamee and the Colebrook and White correlations, as well as the Haaland correlation mentioned in the previous subsection, are expected to give essentially the same results, as they are all equations made to fit the Moody diagram.



+ p90 m600 q10 x p90 m1200 q20 □ p90 m900 q20 Op80 m900 q20 ◇ p9100 m900 q20 Δ p90 m600 q20

Figure 24: Comparison of the measured pressure drop with calculation models

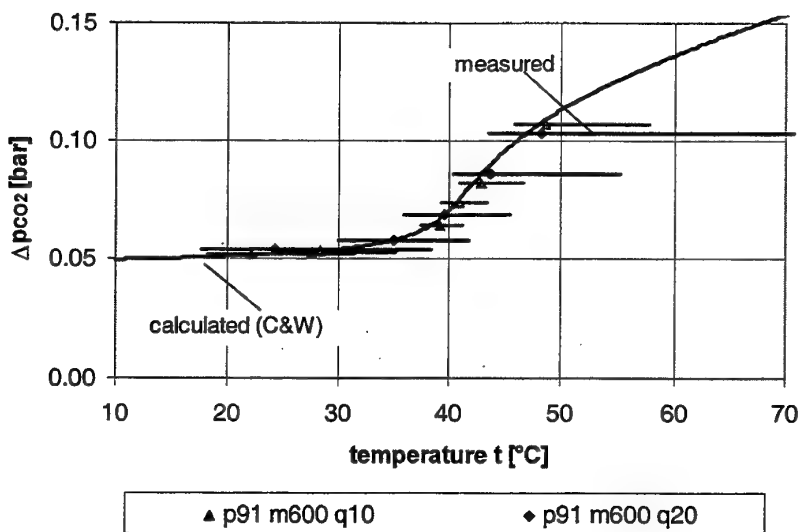


Figure 25: Influence of the heat flux on the pressure drop ($\Delta l = 503$ mm)

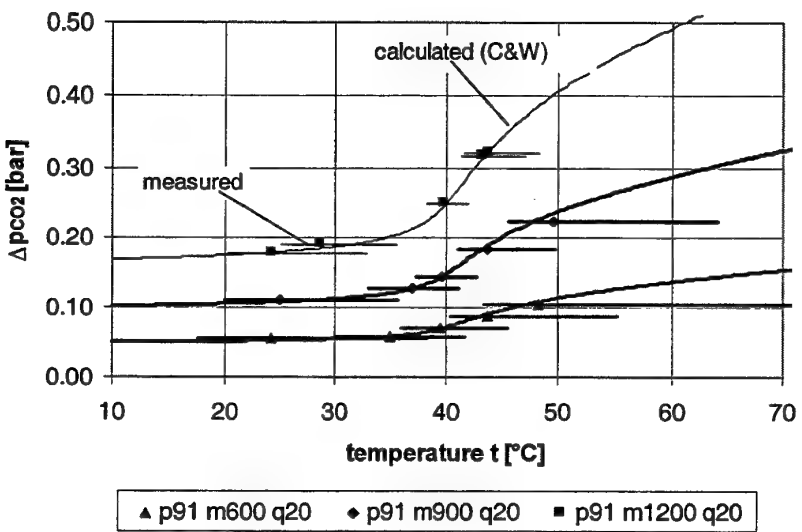
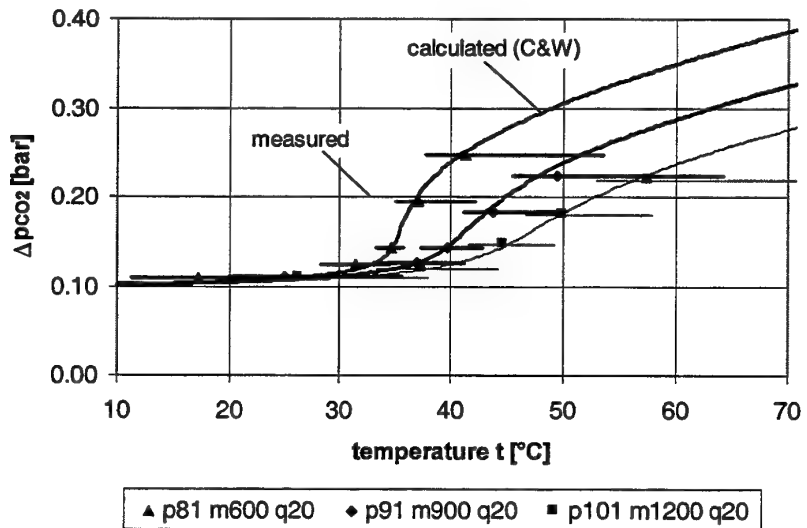


Figure 26: Influence of the mass flow on the pressure drop ($\Delta l = 503$ mm)



5.2 Subcritical Conditions (Evaporation)

5.2.1 General

Even though the critical temperature of CO_2 (31.1°C , 73.8 bar) is quite low, heat absorption takes place at subcritical conditions (evaporation) in heat pump and refrigeration applications. The reduced temperature (T/T_{crit}) and pressure (p/p_{crit}) are quite high, however.

At saturation temperatures between 0 and 20°C , CO_2 has a high vapour density; thus the density ratio between the liquid and vapour phase is significantly lower for CO_2 than for commonly used refrigerants. Furthermore, the surface tension of CO_2 in this important temperature region is very low.

Taking these facts into account, it was decided to analyse the heat transfer and pressure drop characteristics of CO_2 at temperatures between 0 and 20°C . Other reasons for concentrating on this temperature were focusing on air conditioning applications and using water as coolant. Figure 28 shows the evaporation process in a temperature-entropy diagram (see Figure 4 for the flow circuit of the test rig).

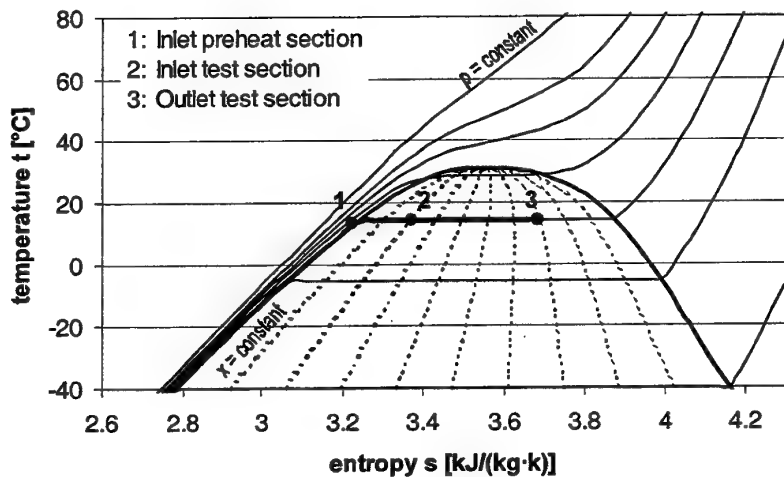


Figure 28: Schematic temperature-entropy diagram with an evaporation process

Slightly sub-cooled liquid entered the preheat section (1), where it was partly evaporated to get the desired vapour fraction at test section inlet (2). In the test section, refrigerant partly evaporated due to the heat supplied by the heat source (water). After leaving the test section (3), refrigerant entered the condenser, where it was condensed to liquid.

In order to determine the influence of mass flux (\dot{m}), the evaporation temperature (t_{evap}), and heat flux (\dot{q}) on the 'local' heat transfer coefficient (α), tests were carried out at different vapour fractions (x_{mean}). Table 6 gives an overview of the test conditions and the experimental tolerances.

Table 6: Test conditions and experimental tolerances during the evaporation tests

Parameter	min	max	max. deviation
\dot{m} (kg/(m ² ·s))	200	600	+6% / -7%
t_{evap} (°C)	0	20	±0.2 K
\dot{q} (W/m ²)	5,000	20,000 ^{*)}	+5% / -10%

^{*)} some tests at higher heat fluxes.

In total, 88 points were collected. Besides the systematic analysis of these data, comparisons with 'common' calculation models were carried out. The results are presented in the following sections.

5.2.2 Heat Transfer at evaporation

In contrast to the supercritical heat transfer coefficient, no specific calculation model for evaporating CO₂ was available in the literature. In [13] it was found that the model proposed by VDI [28] fitted well to the measurements published in [1]. But these measurements were carried out in a tube with an inner diameter of 7 mm. For the present tube this model cannot be applied, because of the small diameter of 0.787 mm.

Six models were chosen for the comparison with the experimental data. Figure 29 shows the quantitative comparison between all measured data and these calculation models, and Table 7 lists the corresponding deviations.

Table 7: Deviation between measured and calculated heat transfer coefficients, all data

Model	Reference	σ_{avg} (%)	σ_{mean} (%)
Slipcevic (1987)	[32]	60	68
Kandlikar (1990)	[33]	49	55
Kattan (1996)	[34]	91	92
Shah (1982)	[35]	4	61
Gungor & Winterton (1986)	[36]	125	56
Gungor & Winterton (1987)	[37]	14	117

As one can see, there was a considerable discrepancy between calculation and experiment. Especially, in case of low measured heat transfer coefficients, the models delivered too high values. If one analyses the data in depth, the major discrepancy is seen to occur at high mass fluxes. Therefore, Table 8 shows the deviations for the points measured at mass fluxes less than or equal to 300 kg/(m²·s). Then the remaining 40 points show a better correspondence. Especially Slipcevic and Kandlikar fitted the measurements very well at low mass fluxes. However, the large deviation at high mass fluxes has to be considered.

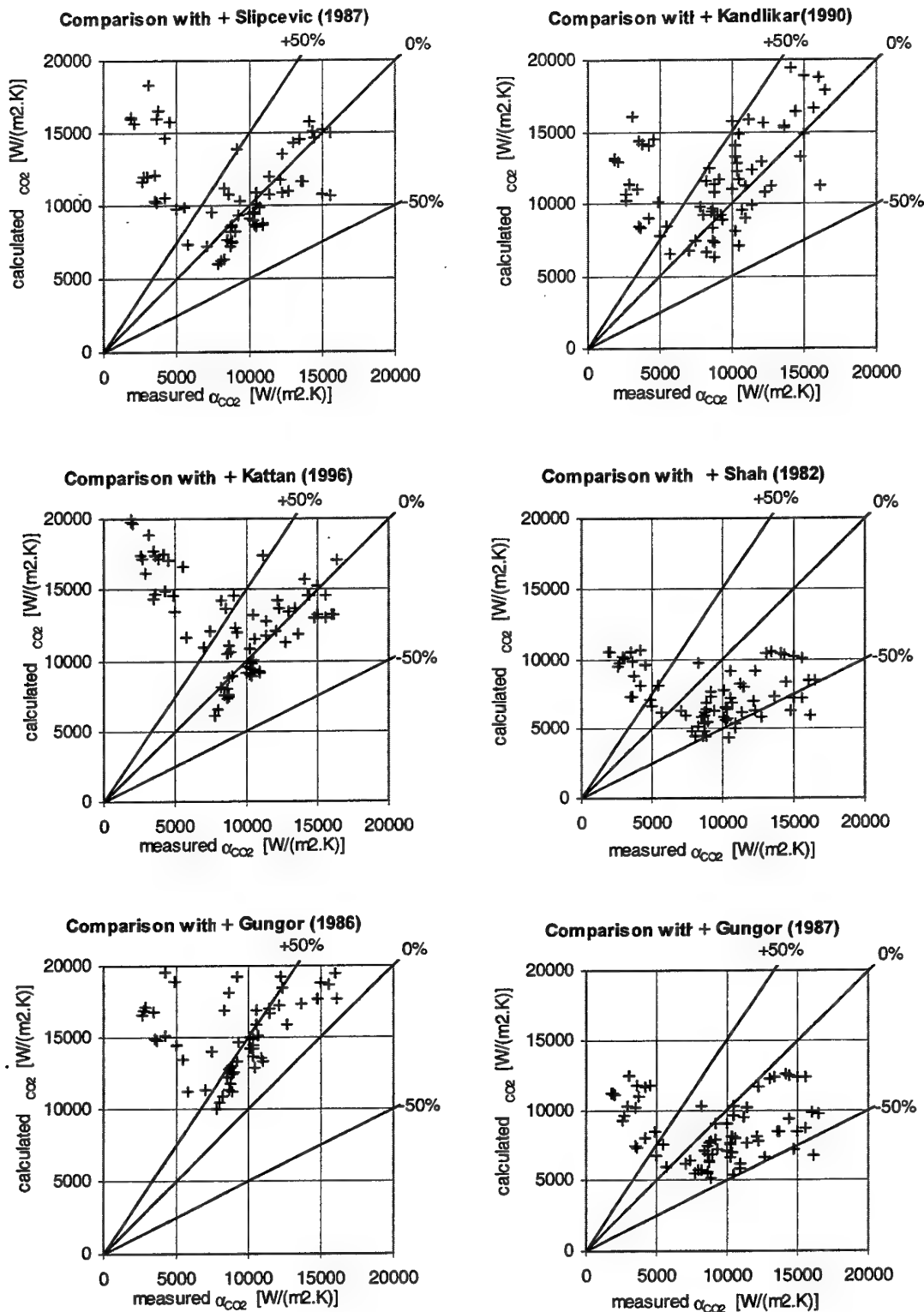


Figure 29: Comparison of measured heat transfer coefficients with calculation models

Table 8: Deviation between measured and calculated heat transfer coefficients, $\dot{m} < 300 \text{ kg}/(\text{m}^2 \cdot \text{s})$

Model	Reference	$\sigma_{\text{avg}} (\%)$	$\sigma_{\text{mean}} (\%)$
Slipcevic (1987)	[32]	-6	15
Kandlikar (1990)	[33]	0	15
Kattan (1996)	[34]	8	22
Shah (1982)	[35]	-41	42
Gungor & Winterton (1986)	[36]	44	44
Gungor & Winterton (1987)	[37]	-33	33

Figure 30 shows the results obtained from the initial evaporation tests. The conditions applied were: $\dot{m} = 600 \text{ kg}/(\text{m}^2 \cdot \text{s})$, $\dot{q} = 20,000 \text{ W}/\text{m}^2$, and different evaporation temperatures. As can be seen, the heat transfer coefficient dropped significantly at high vapour fractions (x). At low vapour fractions it was about $13,000 \text{ W}/(\text{m}^2 \cdot \text{K})$ at 0°C , $15,000 \text{ W}/(\text{m}^2 \cdot \text{K})$ at 10°C , and $22,000 \text{ W}/(\text{m}^2 \cdot \text{K})$ at 20°C evaporation temperature. At vapour fractions higher than 0.55, the measured values were lower than $5,500 \text{ W}/(\text{m}^2 \cdot \text{K})$ for all evaporation temperatures.

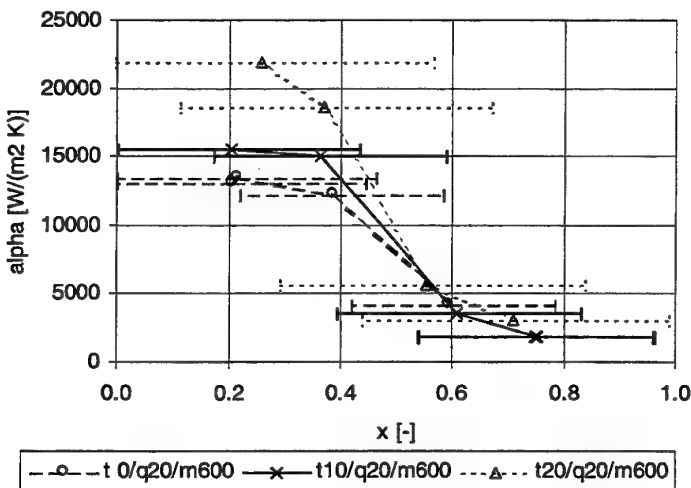


Figure 30: Measured heat transfer coefficients depending on the vapour fraction at a high mass flux (one refrigerant inlet)

Initially, the test section was supplied with CO_2 from one side of the manifold, i.e. an asymmetric flow. This was believed to cause a separation of the liquid and vapour phase in the manifold, which could cause non-uniform supply of liquid to the parallel ports of the test tube. This is shown schematically in Figure 31, which shows a possible solution as well.

It was decided to redesign the manifolds so that the fluid could enter and leave the test section symmetrically, i.e. through two inlets and two outlets. After the reconstruction of the manifolds,

the previous test was repeated at an evaporation temperature of 10°C. Figure 32 shows the result for the 'new' test section (indicated with '2 inlets') in comparison with the 'old' results.

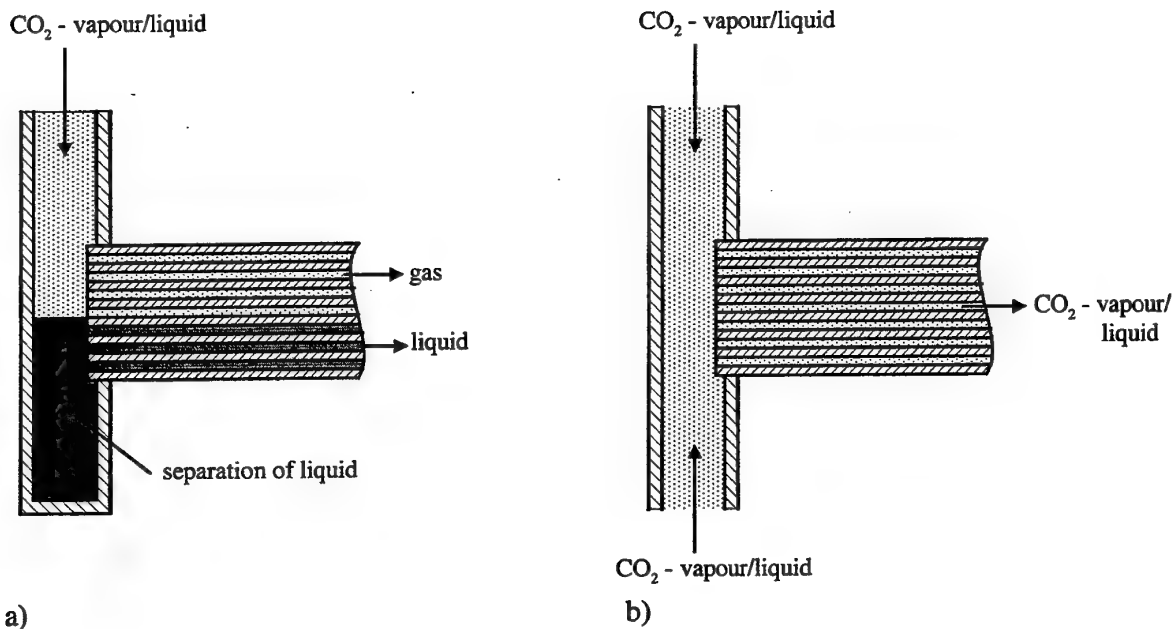


Figure 31: Possible problem and suggested solution

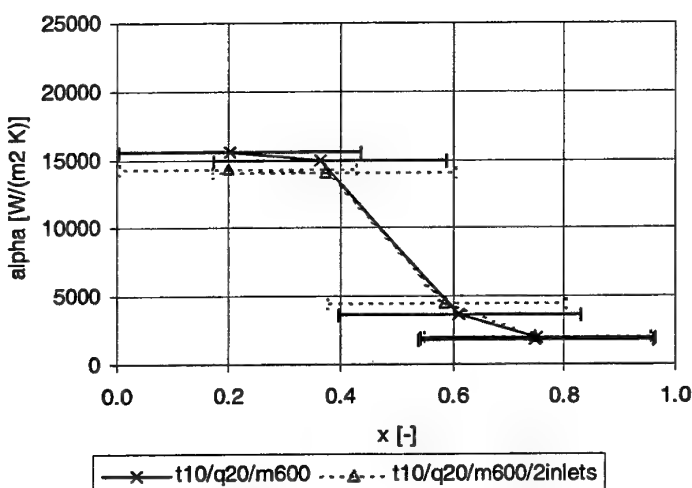


Figure 32: Heat transfer coefficient depending on the vapour fraction at a high mass flux (one vs. two refrigerant inlets)

As can be seen from this figure, there was more or less no change. Thus the conclusion was that the asymmetric design of the inlet gave uniform liquid supply to the ports and the reason for the low heat transfer coefficient at high vapour fractions was yet to be found.

It was decided to run the same test once more, but this time at a reduced heat flux of 5,000 W/m². The result did not change significantly at high vapour fractions, however. To find

out if the high mass flux of $600 \text{ kg}/(\text{m}^2 \cdot \text{s})$ caused this characteristic, a new test series was carried out.

During these tests, the vapour fractions at the inlet and outlet of the test section were kept constant, while the mass flux was changed. This was realised by varying the heat flux. The heat fluxes required to keep the vapour fractions constant were $10,000$ to $26,000 \text{ W}/\text{m}^2$ for the series with an inlet vapour fraction of $x_{in} = 0.3$ and an outlet vapour fraction of $x_{out} = 0.92$, and $14,000$ to $42,000 \text{ W}/\text{m}^2$ for the series with $x_{in} = 0$ and $x_{out} = 0.9$.

Figure 33 shows the result. As can be seen, the influence of the mass flux was significant. At both tests, an increase from 200 to $300 \text{ kg}/(\text{m}^2 \cdot \text{s})$ resulted in a higher heat transfer coefficient. At higher velocities, a significant decrease was observed.

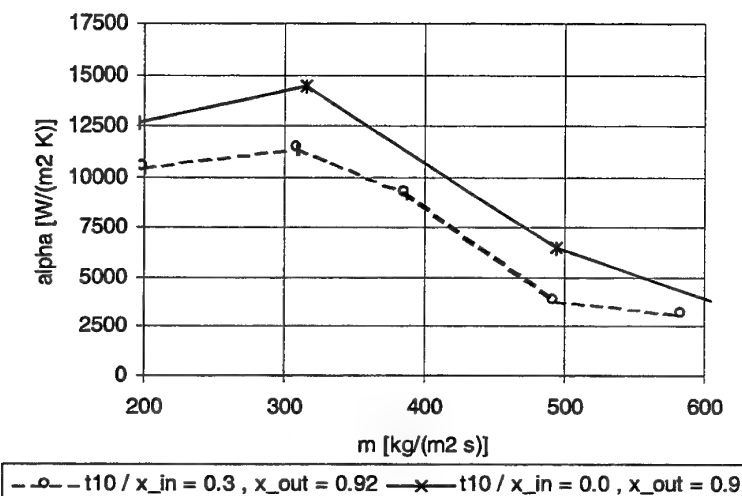


Figure 33: Heat transfer coefficient depending on the mass flux (constant vapour fraction at the inlet and at the outlet)

The higher heat transfer coefficient in case of the lower inlet vapour fraction can be explained by the effect of the heat flux (see below).

A possible explanation for the decreasing heat transfer coefficient with increasing mass flux is the dry-out phenomenon, in which the flow itself causes the liquid which is wetting the wall to be entrained in the core of the flow at high mass fluxes. VDI [28] recommends a rather complicated calculation model for the so-called critical vapour fraction ($x_{critical}$) where dry-out occurs. This model is mainly based on experiments with water. It is required to 'translate' the CO_2 properties into equivalent water properties so that the calculation can be carried out. This was the main reason why it was unclear if this model could be applied for CO_2 .

Figure 34 shows the result of the calculations for different evaporation temperatures (0 , 10 , and 20°C) and heat fluxes ($10,000$ and $20,000 \text{ W}/\text{m}^2$). In case of 20°C saturation temperature and moderate mass fluxes, the figure shows three lines for the critical vapour fraction. In this mass flux range, gravity is expected to influence the dry-out phenomenon. The upper dashed line in

the figure represents the bottom and the lower line the top of the tube. The middle line gives the average value. In other words, dry-out at the top occurs earlier than at the bottom of the tube.

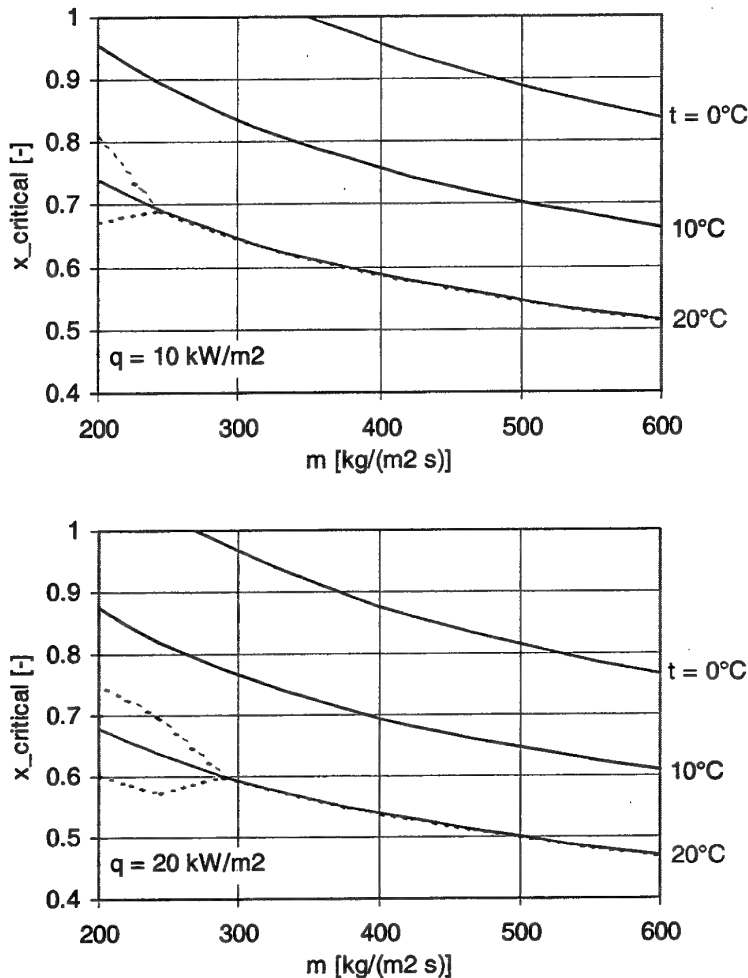


Figure 34: Critical vapour fraction according to VDI [28]

This figure confirms the speculation that dry-out on the heat transferring surface can occur even at rather low vapour fractions. For a mass flux of $600 \text{ kg/(m}^2\text{-s)}$ and a heat flux of $20,000 \text{ W/m}^2$, this model predicts dry-out at a vapour fraction of 0.77 at 0°C , 0.6 at 10°C , and 0.47 at 20°C evaporation temperature. At a mass flux of $300 \text{ kg/(m}^2\text{-s)}$ the corresponding values are 0.96, 0.76, and 0.6, respectively. As may be observed by comparing the first diagram with the second diagram of Figure 34, the lower the heat flux is, the higher the critical vapour fraction becomes.

The measurements shown in Figure 32 completely confirmed the calculation. As the vapour fraction became higher than 0.6, a significant decrease of the heat transfer coefficient occurred. At an evaporation temperature of 0°C the model probably overestimates the critical vapour fraction, as can be seen from a comparison with Figure 30.

Since dry-out is a quite important phenomenon with respect to heat exchanger design, more measurements were needed.

Influence of mass flux:

Tests were carried out at an evaporation temperature of 0°C, 10°C, and 20°C and at mass fluxes of 200, 300, and 400 kg/(m²·s). At all test runs the heat flux was kept constant at 10,000 W/m². Figure 35 shows the results.

From the first diagram (0°C) one can see that at low vapour fractions, neither the mass flux nor the vapour fraction had any influence on the heat transfer coefficient. At all velocities, the measured heat transfer coefficient was about 9000 W/(m²·K). But again, at high vapour fractions and a mass flux of 400 kg/(m²·s), the heat transfer coefficient was significantly reduced.

A similar behaviour can be seen at 10°C (second diagram); at low vapour fractions the heat transfer coefficient was about 10,500 W/(m²·K) and independent of the mass flux. In case of 200 kg/(m²·s) this value was measured at all vapour fractions. But already at 300 kg/(m²·s) and high vapour fractions, a slight drop can be seen. At 20°C (third diagram) and low vapour fractions a value of about 15,000 W/(m²·K) was measured. The drop, however, occurred at lower vapour fractions. These results are – except for the measurement at 20°C / 200 kg/(m²·s) – completely in accordance with the calculated results for the critical vapour fraction presented in Figure 34.

Influence of heat flux:

The influence of heat flux on the heat transfer characteristic of CO₂ is of high interest, as already described in [1]. Within this project, the influence of heat fluxes ranging from 5000 to 15,000 W/m² was investigated. During these experiments, the mass flux was kept constant at 300 kg/(m²·s) while the saturation temperature was varied. In Figure 36 the experimental results are shown.

At 0°C saturation temperature (first diagram), a slightly higher heat transfer coefficient was measured when the heat flux was high. At 10°C (second diagram), the enhancement due to a higher heat flux was larger. At high vapour fractions an exact analysis was not possible because of the different range of vapour fraction of each experiment depending on the heat flux. At 20°C, the change in vapour fraction is large in case of a heat flux of 15,000 W/m². However, the decreased heat transfer coefficient at a high vapour fraction may confirm the fact that due to the higher heat flux, dry-out occurs at a lower vapour fraction. This would mean that the enhancement due to an increased heat flux does not compensate for the drop due to dry-out occurring at a lower vapour fraction.

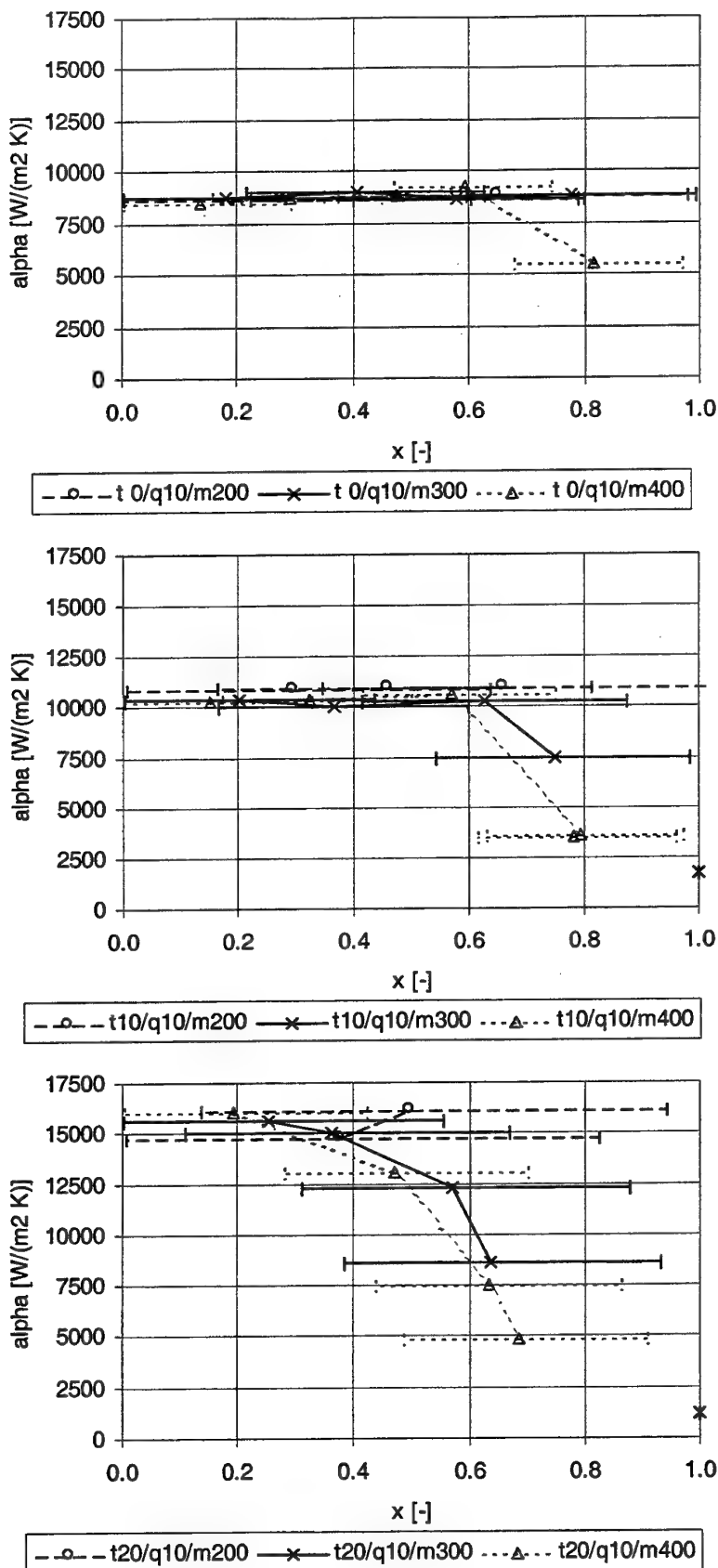


Figure 35: Influence of the mass flux on the heat transfer coefficient at different evaporation temperatures

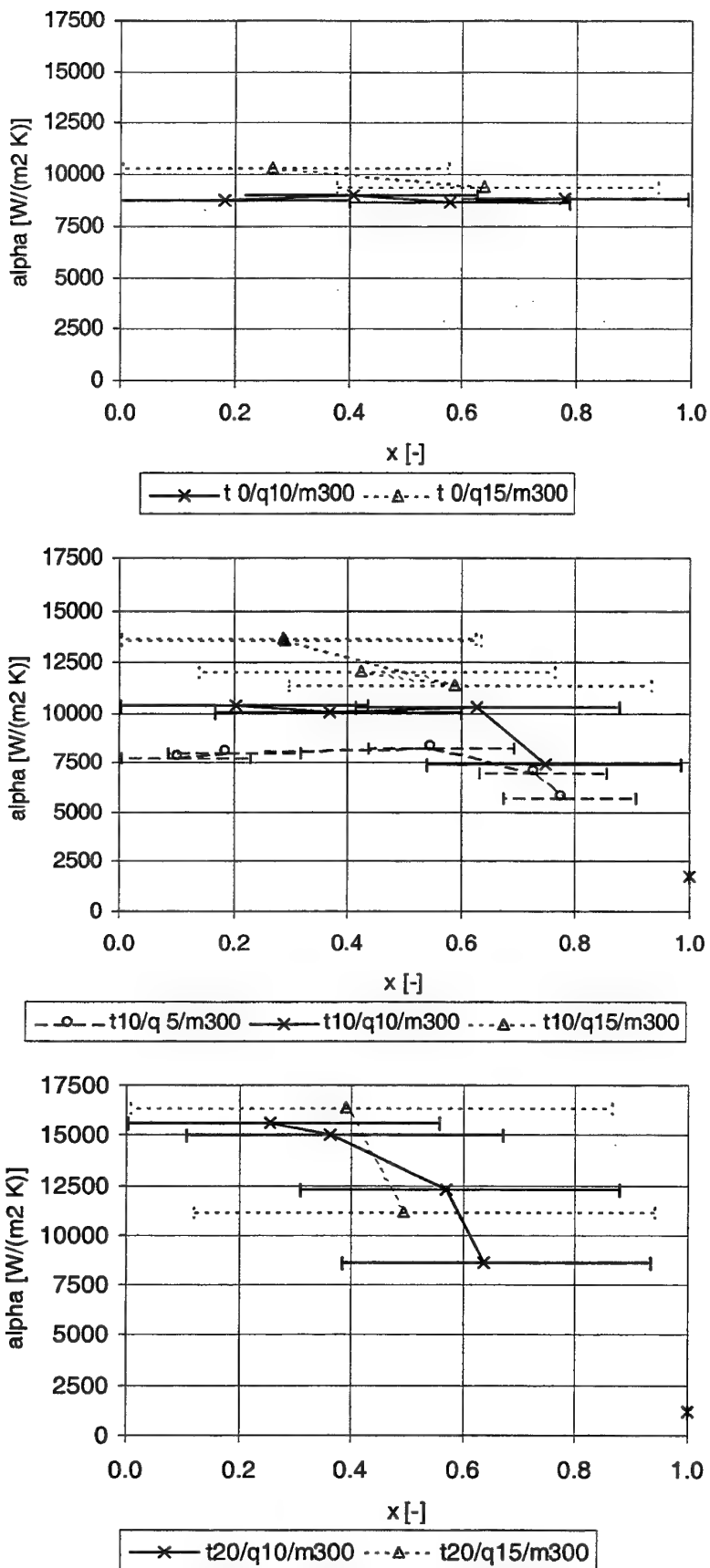


Figure 36: Influence of the heat flux on the heat transfer coefficient at different evaporation temperatures

Influence of evaporation temperature:

The influence of evaporation temperature on the heat transfer characteristics of CO₂ was already mentioned. Figure 37 compares measured heat transfer coefficients at constant heat flux and mass flux, and varying saturation temperature. As may be observed, the heat transfer coefficient was significantly higher for the highest saturation temperature at low vapour fractions. While the heat transfer coefficient was about 9,000 W/(m²·K) at 0°C, it was higher than 15,000 W/(m²·K) at 20°C. At high vapour fractions, the situation is reversed because of the significant drop at high temperatures.

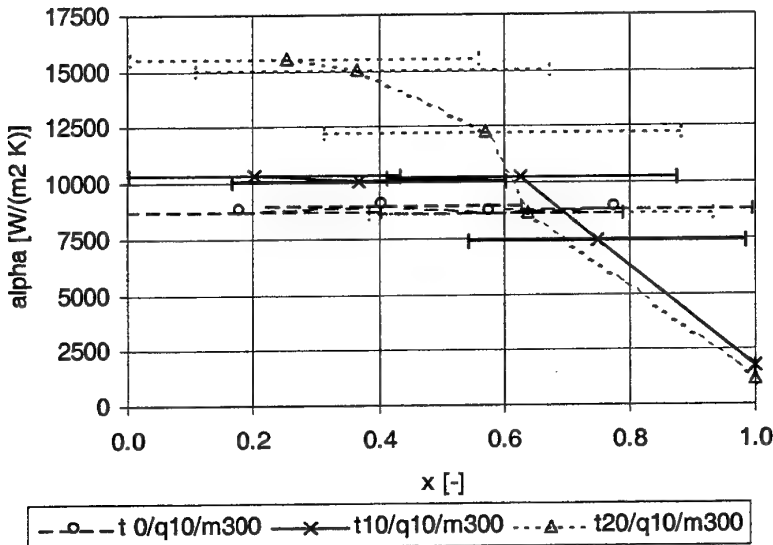


Figure 37: Influence of evaporation temperature on the heat transfer coefficient

5.2.3 Pressure Drop at evaporation

For the comparisons of measured data to calculated values, the following correlations were used:

- Thome (1997): Thome [38] recommended the Friedel correlation using the Premoli approach for the void fraction to calculate the frictional and acceleration pressure drop at evaporation. As shown in [13], this model fits well to measured data carried out in a 7 mm round tube (published by Bredeisen et al in [1]).
- Fuchs&Neraas (1993): Neraas published this model in [39]. It is based on the work of Fuchs [40]. Bredeisen et al. [1] proposed this model for the estimation of the frictional pressure drop of evaporating CO₂.
- VDI (1994): In [28] a rather sophisticated model for the prediction of the pressure drop can be found.
- Single-phase model: This model uses a homogeneous approach by means of the mean density for the two-phase flow. The frictional pressure drop is then calculated for the fictive single-phase flow according to the Colebrook&White correlation [28].

Table 9 shows the resulting deviations, and Figure 38 visualises the fit of the models to the measurements. Thome's recommendation gave the best results. The mean deviation is nevertheless 22%. All other models - and especially the Fuchs&Neraas model that was found to give good correlation to measured data for the 7 mm tube - underestimated the pressure drop significantly.

Table 9: Deviation between measured and calculated pressure drops

Model	Reference	σ_{avg} (%)	σ_{mean} (%)
Thome (1997)	[38]	-7	22
Fuchs&Neraas (1993)	[39]	-56	57
VDI (1994)	[28]	-41	43
Single-phase model	see above	-35	37

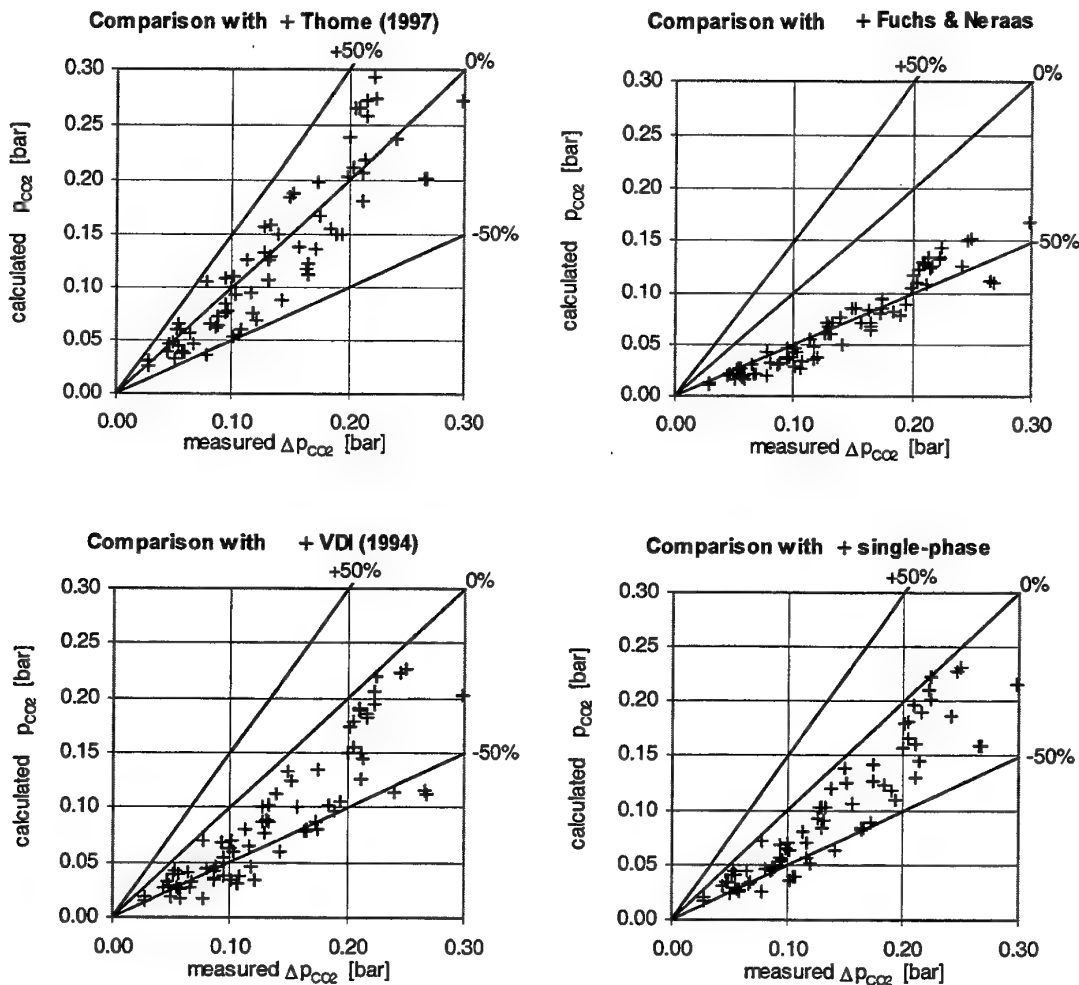


Figure 38: Comparison of measured pressure drop data with calculation models

In the following figures, some of the measured data are compared with the results calculated according to Thome [38].

The influence of mass flux on the pressure drop at a saturation temperature of 10°C can be seen in Figure 39. While the measurements at 200 kg/(m²·s) showed a moderate pressure drop at all vapour fractions, the pressure drop at 400 kg/(m²·s) increased significantly with the vapour fraction. As one can see, the calculated values did not correlate very well to the experimental data. Especially at low vapour fractions the deviation was high.

Finally, Figure 40 shows the influence of the saturation temperature on the pressure drop. The mass flux was constant at 300 kg/(m²·s) during these tests. With decreasing saturation temperature, the vapour volume increases, and this is the main reason for the remarkably higher pressure drop at 0°C compared to that at 20°C. Regarding the deviation between measurement and calculation, one can see that the model underestimates the pressure drop in case of low temperatures.

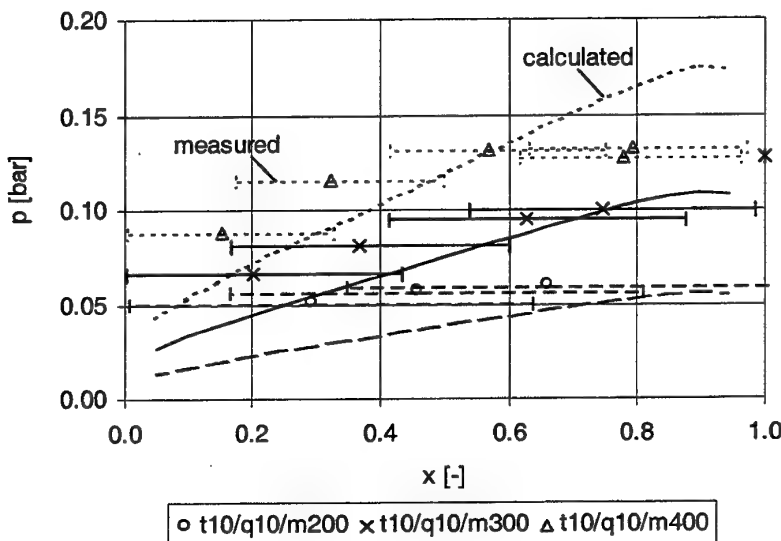


Figure 39: Influence of the mass flux on the two-phase pressure drop ($\Delta l = 503$ mm)

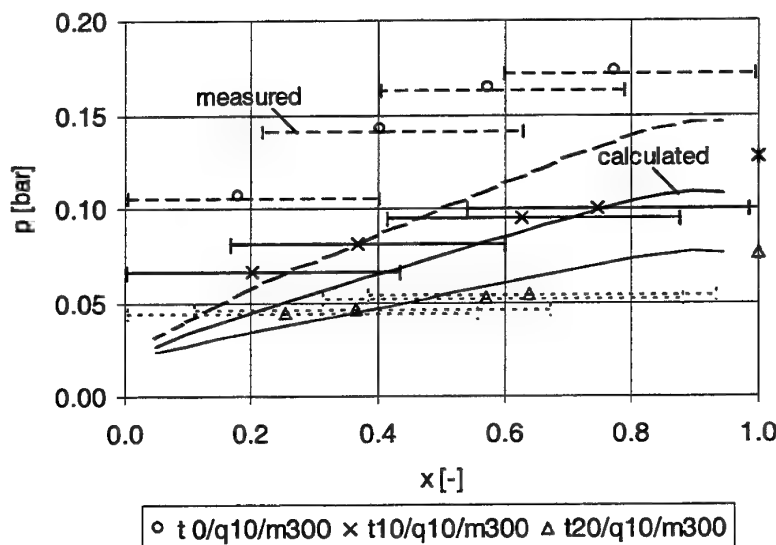


Figure 40: Influence of the saturation temperature on the two-phase pressure drop ($\Delta l = 503$ mm)

6 ASSESSMENT OF RESULTS

In this chapter, the evaporation heat transfer data presented in the previous chapter will briefly be assessed regarding their consequences for the design of CO₂-based air conditioning systems. It will be done by means of comparing previous capacity measurements of evaporators conducted in the laboratory at SINTEF Energy Research with calculations of evaporators using correlations and the heat transfer data obtained in this work.

6.1 Previous evaporator measurements

In a previous project, the performance of vehicle air conditioning evaporators were measured. The prototype evaporator consisted of extruded aluminium multiport tubes of similar geometry to the one used in the present work. A photograph of the evaporator is shown in Figure 41.

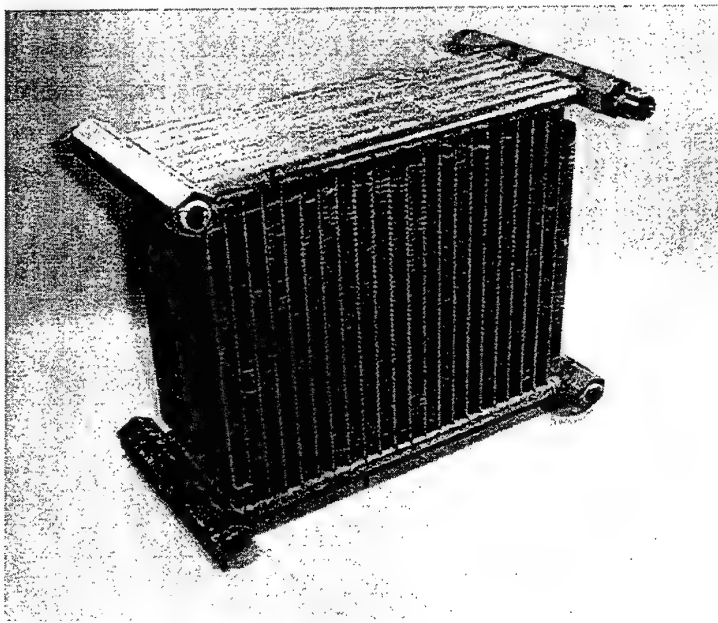


Figure 41: Prototype automotive aluminium multiport extruded tube evaporator.

The evaporator inlet air temperature ranged from 26–48 °C, the inlet relative air humidity was varied between 29 and 28 % and the air flowrate was between 386 and 394 Sm³/h.

The CO₂ mass flux ranged from 270 to 900 kg/(m²s) (it also varied internally in the evaporator due to the varying number of parallel tubes). The evaporation temperature varied from –1 to 15 °C and the heat flux ranged from 3,500 and 10,000 W/m².

6.2 Evaporator simulations

The computer program HXSIM was developed at SINTEF Energy Research to assist the design of compact evaporators, gas coolers and condensers. It simulates the heat exchangers considering a great range of parameters.

Simulations of the test cases mentioned in the previous section were performed with three different calculation methods for the CO₂-side heat transfer coefficient:

1. The CO₂-side heat transfer coefficient was calculated with the simplified Gungor and Winterton (1987) correlation [37]. (The Kandlikar (1990) correlation was not implemented in HXSIM).
2. The CO₂-side heat transfer coefficient was calculated with the simplified Gungor and Winterton (1987) correlation, but the drop in heat transfer coefficient due to dry-out was accounted for by the following modification: For vapour fractions larger than the critical vapour fraction given by VDI [28], the nucleation boiling factor (boiling number) was set to zero. Then the effective heat transfer coefficient was calculated as outlined in [41].
3. The CO₂-side heat transfer coefficient was based on the experimental data presented in this work. For each of the evaporator test points, a heat transfer curve for a suitable evaporation temperature and mass flux was found. Then the heat transfer coefficient was given as a function of vapour fraction to the HXSIM program. The HXSIM program thus used one-dimensional interpolation of the test data to find the CO₂-side heat transfer coefficient when simulating the evaporator.

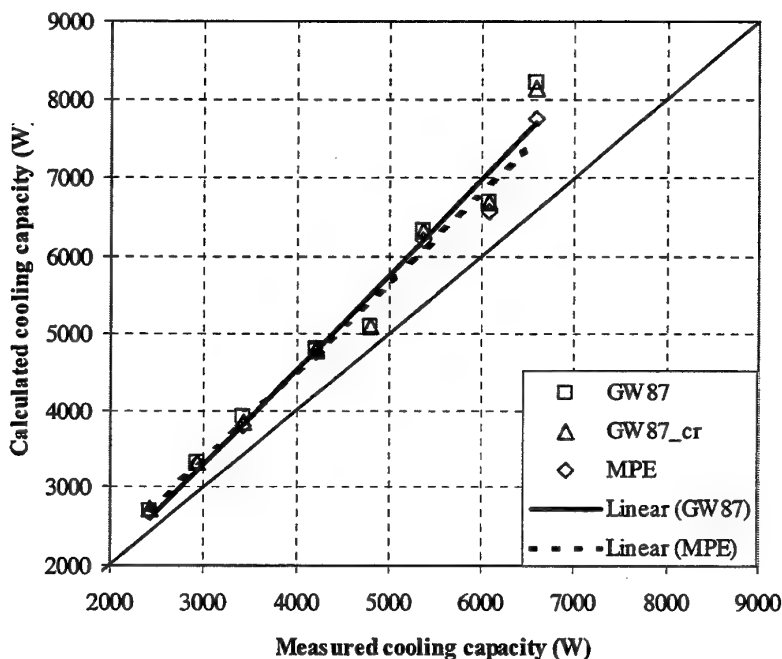


Figure 42: Measured and calculated cooling capacities of MPE evaporator.

The symbols are explained in the text

The results of the calculations are shown in Figure 42. The capacities calculated using the Gungor and Winterton (1987) correlation (labelled GW87) all lay above the measured values. The thick line is a linear curve-fit to these values. At 6,000 W capacity, GW87 yielded a capacity 17 % higher than the measured one. GW87_cr denotes the Gungor and Winterton (1987) correlation modified to take account for the drop in the heat transfer coefficient caused by dry-out. These values lay only slightly lower than the GW87 values. The capacities obtained using the measured heat transfer data are labelled MPE. The dotted line is a linear curve-fit through these points. At 6,000 W, the MPE data yielded a capacity 14 % higher than measured, i.e. 3 percentage points lower than what was given by GW87.

6.3 Discussion

The evaporator cooling capacities obtained using measured MPE heat transfer data were only slightly lower than those obtained using the Gungor and Winterton (1987) correlation. This is perhaps surprising, having seen in the previous chapter that the average deviation between this correlation and the measured heat transfer coefficients was 14 %, and that the mean deviation was as high as 117 %. Generally one may assume the possible discrepancy between calculated and measured heat transfer coefficients to be in the range of 20 %.

The most important reason for the small differences between the calculated evaporator capacities for different CO₂-side heat transfer coefficients, was that as much as around 80 % of the heat transfer resistance was on the air-side. Thus one can roughly say that a 20 % increase in the CO₂-side heat transfer coefficient only results in a 4 % increase in the transferred heat.

The most important cause for most of the heat transfer resistance being on the air-side was that the heat transfer coefficient on the CO₂-side was very high, together with the fact that the ratio between the air-side surface and the CO₂-side surface was quite low. A different refrigerant and/or different operating conditions leading to a lower refrigerant-side heat transfer coefficient would, therefore, result in variations in the refrigerant-side heat transfer coefficient having a greater influence on the evaporator cooling capacity than seen in this comparison.

Important reasons for the about 15 % deviation between simulated and measured evaporator performance include:

- Effects of retained water on the air-side.
- Presence of lubricant in the refrigerant flow.

The evaporator discussed here was a prototype with a rather small air-side area compared to that on the CO₂-side ($A_{\text{air}}/A_{\text{CO}_2} = 6$). Later evaporators would probably be constructed with a larger air-side area, thus approaching an equal distribution of the heat transfer resistances between the two sides. In such an instance, a 20 % increase in the CO₂-side heat transfer coefficient would lead to a roughly 10 % increase in the transferred heat, which is not insignificant. The same would be the case for e.g. a water-heated evaporator, where heat transfer coefficients on both sides would be high.

7 CONCLUSIONS

Within this project, the heat transfer and pressure drop characteristic of CO₂ (R-744) was investigated. The focus was on the heat rejection process at supercritical pressures and the heat absorption process at subcritical pressures (evaporation). The test tube was a so-called MultiPort Extruded tube with micro-channels. It had 25 parallel ports on the refrigerant-side with a port diameter of 0.787 mm.

Because of the low critical temperature of CO₂ (31°C), the so-called transcritical vapour compression cycle will be used in several applications, including U.S. Army Environmental Control Units. Therefore, the test conditions were selected in order to collect knowledge on near-critical processes.

In the transcritical cycle, refrigerant is cooled at supercritical pressure, where the influence of the critical point on the properties is quite large, and it evaporates at temperatures close to the critical temperature, where the high saturation pressure results in high vapour densities. Furthermore, the surface tension of CO₂ is very low. These factors lead to conditions in CO₂ equipment differing considerably from those of the hitherto commonly used refrigerants.

The experimental results confirm that CO₂ offers high heat transfer coefficients at super-critical pressures. A comparison of these data with common correlations showed good correspondence. Especially the Nusselt number based on the Gnielinski correlation in combination with Haaland's friction factor correlated very well with the experimental data. This model can be found in the Appendix.

The pressure drop of CO₂ to be expected in a refrigerant cooler is rather high, but due to the high pressure level, the effect on temperature loss is moderate [13]. A comparison of the experimental data with calculations using the Colebrook & White correlation showed satisfactory agreement. This model is also outlined in the Appendix.

The heat transfer characteristics of CO₂ during evaporation is not as clear as the situation at supercritical pressures. The effect of the low density ratio between liquid and vapour may significantly affect the two-phase flow. In case of high mass fluxes, the experiments showed a strongly decreasing heat transfer coefficient from a certain vapour fraction upwards. In the temperature region investigated, the 'critical' mass flux was about 300 kg/(m²·s), with some variation depending on the saturation temperature and the heat flux. A comparison with a calculation model for dry-out showed that this drop had to be expected. The calculated values for the critical vapour fraction corresponded well to the observations. This very important fact has to be considered when designing evaporators.

None of the investigated heat transfer calculation models takes this phenomenon into account. If the measurements at high mass flow rates were not included, the models proposed by Slipcevic and by Kandlikar yielded sufficient accuracy. Kandlikar's model is given in the Appendix. However, regarding the qualitative accuracy of this model, one has to remember that only measured mean values have been compared with the calculation results.

The two-phase pressure drop correlations yielded too low values in general. The calculation model proposed by Thome, the Friedel correlation for the frictional pressure drop, and Premoli's approach for the void fraction (see Appendix), can be used for a rough estimation of the pressure drop to be expected. But at low temperatures and low vapour fractions, the calculated values were significantly lower than the measured ones. A model used for calculating the pressure drop in a 7 mm round tube could not be used for predicting the pressure drop in the micro-channel tube that was investigated within this project.

A variation in the CO₂-side heat transfer coefficient had only a minor influence on the evaporator capacity of a prototype automobile air conditioning evaporator considered in this work. On this evaporator, most of the heat transfer resistance lay on the air-side. For evaporators with a more evenly distributed heat transfer resistance between the CO₂-side and 'the other' side, however, a change in the CO₂-side heat transfer coefficient will have an effect on the evaporator capacity.

All the results achieved within this project are important for the design of CO₂ heat exchangers. Especially the influence of the mass flux and dry-out on the two-phase heat transfer characteristics has to be taken into consideration in further work.

BIBLIOGRAPHY

- [1] Leister, A.: Experimental Study on Heat Transfer and Pressure Drop in Extruded and Drawn Tubes for Compact Heat Exchangers. Diplomarbeit Nr. 99-29, Fachhochschule Karlsruhe, Germany (carried out at SINTEF Energy Research, Trondheim, Norway), 1999.
- [2] Bredesen, A.M., Hafner, A., Pettersen, J., Neksa, P., Aflekt, K.: Heat Transfer and Pressure Drop for In-tube Evaporation of CO₂. Proc. IIR Conference: Heat Transfer Issues in 'Natural' Refrigerants, University of Maryland, USA, p. 35 – 49, 1997.
- [3] Lorentzen, G.: The Use of Natural Refrigerants: A Complete Solution to the CFC/HCFC Predicament. *International Journal of Refrigeration*. Vol 18 No 3, pp 190-197, 1995.
- [4] Pettersen, J.: An Efficient New Automobile Air-Conditioning System based on CO₂ Vapor Compression. ASHRAE Annual Meeting. *ASHRAE Transactions* Vol 100 Part 2, pp 657-665, 1994.
- [5] Pettersen, J.: Experimental Results of Carbon Dioxide in Compression Systems. Conference "Refrigerants for the 21st Century" organized by ASHRAE/NIST, Gaithersburg, Maryland, USA. October 6-7. Proceedings pp.27-37, 1997.
- [6] Pettersen, J., Skaugen, G.: Operation of Trans-Critical CO₂ Vapour Compression Circuits in Vehicle Air Conditioning. Proc. IIR Conference: *New Applications of Natural Working Fluids in Refrigeration and Air Conditioning*. Hannover, Germany, May, pp 495-505, 1994.
- [7] Hafner, A., Pettersen, J., Skaugen, G., Neksa, P.: An Automobile HVAC System with CO₂ as the Refrigerant. *IIR Gustav Lorentzen Conference Natural Working Fluids '98*, Oslo Norway, June 2-5, 1998.
- [8] Neksa, P., Rekstad, H., Zakeri, G.R.: CO₂ Prototype Hot Water Heat Pump. Characteristics, system design and experimental results. Proc. IIR meeting, Heat Pump Systems, Energy Efficiency and Global Warming, Linz, Austria, 28. September - 1. October, 1997.
- [9] Pettersen, J., Aarlien, R., Neksa, P., Skaugen, G., Aflekt, K.: A Comparative Evaluation of CO₂ and R-22 Residential Air-Conditioning Systems in a Japanese Climate. *IEA/IIR Workshop on CO₂ Technologies in Refrigeration, Heat Pump and Air Conditioning Systems*, Trondheim, Norway, May 13-14, 1997.

[10] Manzione, J.A.: Development of Carbon Dioxide Environmental Control Unit for the US Army. *IIR Gustav Lorentzen Conference Natural Working Fluids '98*, Oslo Norway, June 2-5, 1998.

[11] Pettersen, J., Hafner, A., Skaugen G., Rekstad, H.: Development of compact heat exchangers for CO₂ air-conditioning systems. *International Journal of Refrigeration*, Vol 21, No 3, pp. 180-193, 1998.

[12] UNEP: Montreal Protocol on Substances that Deplete the Ozone Layer. 1994.

[13] Rieberer, R.: CO₂ as Working Fluid for Heat Pumps. Ph.D. thesis, Graz University of Technology, Graz, December 1998.

[14] Mills, A. F.: Heat Transfer. Prentice-Hall, Inc., New Jersey, second edition, 1999.

[15] Tang, H. K.: Differences in calculation method of the heat transfer coefficient k. Internal report, SINTEF Energy Research, Trondheim, Norway, 1998.

[16] Database gclib.dll, developed at SINTEF Energy Research

[17] Kays, W. M., London, A. L.: Compact Heat Exchangers. Third edition, McGraw-Hill Book Company, New York, 1984.

[18] Collier, J. G., Thome, J. R.: Convective Boiling and Condensation. Third edition, Clarendon Press, Oxford, 1994.

[19] Yang, Y. C., Webb, R. L.: Friction pressure drop of R-12 in small hydraulic diameter extruded aluminum tubes with and without micro-fins. *International Journal of Heat and Mass Transfer*, Volume 39, No. 5, pages 281-809, 1996.

[20] Akers, W. W., Deans, H. A., Crosser, O. K.: Condensing heat transfer within horizontal tubes. *Chemical engineering progress symposium series*, Volume 55, No. 29, pages 171-176, 1959.

[21] Munkejord, S. T., Hafner, A.: Heat Transfer Capability Measurements of Aluminium Multiport Extruded Tubes. Technical Report, SINTEF Energy Research, Trondheim, July 1998.

[22] Dossou-Yovo, F. A.: Rebuilding of a multiport extruded tubes heat exchanger test rig. Technical report, SINTEF Energy Research, Trondheim, September 1998.

- [23] Wilson, E. E.: A basis for rational design of heat transfer apparatus. Transaction of the ASME (Journal of heat transfer), volume 37, pages 47-82, 1915.
- [24] Farrell, P., Wert, K., Webb, R.: Heat transfer and friction characteristics of turbulator tubes. SAE Transactions, Volume 100, No. 5, pages 218-230, 1991.
- [25] Munkejord S. T.: Varmeovergang og trykktap i ekstruderte multiportrør. Master's thesis, Norges teknisk-naturvitenskapelige universitet NTNU, Trondheim, 1997.
- [26] Beitz, W., Grote, K. H: Dubbel - Taschenbuch für den Maschinenbau. 19. Auflage, Springer Verlag, Berlin, 1997.
- [27] Hwang, Y, Kim, B. H., Radermacher, R.: Boiling Heat Transfer Correlation for Carbon Dioxide. Heat Transfer Issues in 'Natural' Refrigerants, Volume 1, University of Maryland, Maryland, 1997.
- [28] VDI Wärmeatlas: Berechnungsblätter für den Wärmeübergang. 7. Auflage, VDI Verlag, Düsseldorf, Germany, 1994.
- [29] Polyakov, A. F.: Heat Transfer under Supercritical Pressures. Advances in Heat Transfer, Volume 21, Academic Press, pages 1-51, 1991.
- [30] Ghajar A.T, Asadi A.: Improved Forced Convective Heat Transfer Correlation for Liquids in the Near Critical Region. AIAA Journal Vol. 24, No 12, p. 2030 –2037, 1986.
- [31] Swamee P.K., Jain A.K.: Explicit Equations for Pipe-Flow Problems. Journal of the hydraulic division, Proc. of the American Society of Civil Engineers, Vol.102, No.HY5, p. 657-664, 1975.
- [32] Slipcevic B.: Neues über den Wärmeübergang beim Sieden in glatten waagerechten Rohren. KI Klima-Kälte-Heizung, No.1, Germany, p. 31 – 34, 1987.
- [33] Kandlikar S.G.: A General Correlation for Saturated Two-phase Flow Boiling Heat Transfer Inside Horizontal and Vertical Tubes. ASME Journal of Heat Transfer, Vol. 112, p. 219 – 228, 1990.
- [34] Kattan N.: Contribution to the Heat Transfer Analysis of Substitute Refrigerants in Evaporator Tubes with Smooth or Enhanced Tube Surfaces. Thèse N°1498, École polytechnique fédérale de Lausanne, Switzerland, 1996.

[35] Shah, M.M.: Chart Correlation for Saturated Boiling Heat Transfer: Equations and Further Study, ASHRAE Transactions, Vol. 88, Part 1, p. 185 – 196, 1982.

[36] Gungor, K. E., Winterton, R.H.S.: A General Correlation for Flow Boiling in Tubes and Annuli. Int. J. Heat Mass Transfer, Vol. 29, No. 3, p. 351 – 358, 1986.

[37] Gungor, K.E., Winterton, R.H.S.: Simplified general correlation for saturated flow boiling and comparisons of correlations with data. The Canadian Journal of Chemical Engineering (Chem Eng Res Des), Vol. 65, No. 1, pp. 148–156, 1987.

[38] Thome, J.R.: Refrigeration Heat Transfer. Course notes, GRETh/CEA, Grenoble, France, 1997.

[39] Neraas, B.: Condensation of Hydrocarbon Mixtures in Coil-wound LNG Heat exchangers. Tube-side Heat Transfer and Pressure Drop. Ph.D. thesis, Department of Refrigeration Engineering, NTNU Trondheim, Norway, 1993.

[40] Fuchs P.H: Trykkfall og varmeovergang ved strømning av fordampende væske i horisontale rør og bønd. Ph.D. Thesis, Department of Refrigeration, NTH, Trondheim, Norway, 1975.

[41] Mathur, G.D.: Modeling and Simulation of Thermal and Hydrodynamic Performance of Heat Exchangers for Automotive Applications – Part II: Evaporators. Paper no. 970830, New Developments in Heat Exchangers for Automotive Design (SP-1262), SAE, 1997.

[42] Angus, S., Armstrong, B. and DeReuck, K.M.: Carbon Dioxide – International Thermodynamic Tables of the Fluid State, Pergamon Press, 1976.

[43] Pitzer, K.S. and Schreiber, D.R.: Improving Equations-of-state Accuracy in the Critical Region; Equations for Carbon Dioxide and Neopentane as Examples. Fluid Phase Equilibria, vol. 41, pp. 1–17, 1988.

[44] Vesovic, V., Wakeham, W.A., Olchowy, G.A., Sengers, J.V., Watson, J.T.R. and Millat, J.: The Transport Properties of Carbon Dioxide. J.Phys.Chem.Ref.Data, vol. 19, no. 3, pp.763–808, 1990.

NOMENCLATURE

Symbols	Description	Formula	Unit
<i>A</i>	Area, surface	-	m^2
<i>A</i>	Wilson Plot constant (slope)	-	-
<i>B</i>	Wilson Plot constant (intersection)	-	-
<i>Bo</i>	Boiling number	-	-
<i>C</i>	Constant	-	-
<i>C_c</i>	Coefficient of contraction	-	-
<i>Co</i>	Convective number	-	-
<i>c_p</i>	Specific isobaric heat capacity	-	$\text{J}/(\text{kg}\cdot\text{K})$
<i>D</i>	Log. Wilson Plot constant (slope)	-	-
<i>d_{hyd}</i>	Hydraulic diameter	-	m
<i>E</i>	Log. Wilson Plot constant (intersection)	-	-
<i>F, G, H</i>	Factor		
<i>F_α</i>	Property factor	$F_{\alpha} = 0.023 \cdot \text{Pr}^{0.4} \cdot \lambda / \eta^{0.8}$	-
<i>f</i>	Friction factor	-	-
<i>Fr</i>	Froude number		
<i>g</i>	Gravity	-	m/s^2
<i>h</i>	Specific enthalpy	-	J/kg
<i>h'</i>	Specific enthalpy of saturated liquid	-	J/kg
<i>h''</i>	Specific enthalpy of saturated gas	-	J/kg
<i>k</i>	Overall heat transfer coefficient	-	$\text{W}/(\text{m}^2 \cdot \text{K})$
<i>K_c</i>	Entrance pressure loss coefficient	-	-
<i>K_e</i>	Exit pressure loss coefficient	-	-
<i>m</i>	Reynolds exponent	-	-
<i>ṁ</i>	Specific mass flow, mass flux	$\dot{m} = \dot{M}/A$	$\text{kg}/(\text{m}^2 \cdot \text{s})$
<i>Ṁ</i>	Mass flow rate	-	kg/s
<i>n</i>	Prandtl exponent	-	-
<i>n</i>	Number of cells	-	-
<i>Nu</i>	Nusselt number	$Nu = (\alpha \cdot d_{hyd}) / \lambda$	-
<i>p</i>	Pressure	-	Pa, bar
<i>Pr</i>	Prandtl number	$\text{Pr} = c_p \cdot \eta / \lambda$	-
<i>q̇</i>	Heat flux	$\dot{q} = \dot{Q}/A$	W/m^2
<i>Q̇</i>	Heat transfer rate	-	W
<i>Re</i>	Reynolds number	$Re = \dot{m} \cdot d_{hyd} / \eta$	-
<i>R_w</i>	Heat transfer resistance	-	$(\text{m}^2 \cdot \text{K})/\text{W}$
<i>s</i>	Specific entropy	-	$\text{J}/(\text{kg} \cdot \text{K})$
<i>t</i>	Temperature	-	$^{\circ}\text{C}$

Symbols	Description	Formula	Unit
\bar{t}	Mean temperature	-	°C
T	Absolute temperature	-	K
t_{pseudo}	Pseudo-critical temperature	-	°C
v	Specific volume	$1/\rho$	m^3/kg
We	Weber number	-	-
x	Vapour fraction	$x = (h - h')/(h'' - h')$	-
X_1	Independent variable of Wilson Plot	-	-
X_2	Independent variable of log. Wilson Plot	-	-
Y_1	Dependent variable of Wilson Plot	-	-
Y_2	Dependent variable of log. Wilson Plot	-	-
α	Heat transfer coefficient	$\alpha = q \cdot / t_w - t $	$\text{W}/(\text{m}^2 \cdot \text{K})$
Δ	Difference	-	-
ε	Void fraction	-	-
ε	Roughness of the tube surface	-	m
Φ	Two-phase multiplier	-	-
η	Dynamic viscosity	-	$\text{Pa} \cdot \text{s}$
λ	Friction factor	-	-
λ	Thermal conductivity	-	$\text{W}/(\text{m} \cdot \text{K})$
ρ	Density	-	kg/m^3
σ	Ratio of port area to front area	$\sigma = A_{p,tot} / A_{fr}$	-
σ	Surface tension	-	N/m
ξ	Friction factor	-	-

Subscripts	Description
c	cold fluid
c	contraction
$calc$	calculated
con	post condenser
con	condenser
$cool$	cooling
$cooler$	water cooler
e	expansion
el	electrical
eq	equivalent
fl	fluid

Subscripts	Description
<i>evap</i>	evaporation
<i>f</i>	friction
<i>fr</i>	front
<i>g</i>	gas
<i>h</i>	heat exchanger
<i>h</i>	hot fluid
<i>heat</i>	heating
<i>h</i>	homogeneous
<i>hyd</i>	hydraulic
<i>i</i>	inner
<i>i</i>	inlet
<i>i</i>	cell i
<i>ips</i>	inlet preheat section
<i>its</i>	inlet test section
<i>l</i>	liquid
<i>lm</i>	logarithmic mean
<i>m</i>	mean
<i>meas</i>	measured
<i>mps</i>	middle of preheat section
<i>o</i>	outer
<i>o</i>	outlet
<i>ots</i>	outlet test section
<i>p</i>	port
<i>ref</i>	refrigerant
<i>spec</i>	specific
<i>tot</i>	total
<i>ts</i>	test section
<i>w</i>	wall
<i>w</i>	water flow
<i>w</i>	water

APPENDIX : CORRELATIONS

A.1 Super-critical Conditions (Cooling)

A.1.1 Heat Transfer

The mean Nusselt number for turbulent flow in a tube ($2,300 < Re < 1 \cdot 10^6$) can be calculated according to Gnielinski's correlation VDI (1994):

$$Nu_m = \frac{\frac{f}{8} \cdot (Re - 1000) \cdot Pr}{1 + 12.7 \cdot \sqrt{\frac{f}{8} \cdot (Pr^{2/3} - 1)}} \cdot \left[1 + \left(\frac{d}{l} \right)^{2/3} \right] \quad \text{Eq 1}$$

where l is the tube length, and f is the pressure drop factor. Here the measurements justify the use of Haaland's friction factor (Munkejord, 1998):

$$f = \left\{ -1.8 \cdot \log \left[\frac{6.9}{Re} + \left(\frac{\epsilon/d}{3.7} \right)^{1.11} \right] \right\}^{-2} \quad \text{Eq 2}$$

where ϵ is the tube roughness. Comparisons have shown a good correspondence of this correlation to the well-known Colebrook & White correlation (Eq 5).

The influence of the temperature on the properties can be taken into account by

$$Nu = Nu_m \cdot \left(\frac{Pr}{Pr_w} \right)^{0.11} \quad \dots \text{for liquids} \quad \text{Eq 3}$$

where Pr is the Prandtl number at the average fluid temperature and Pr_w is the Prandtl number of the fluid at wall temperature (range of validity $0.1 < Pr/Pr_w < 10$). Since there is no noticeable influence of temperature on the Prandtl number in the case of gaseous fluids, the influence is taken into account by

$$Nu = Nu_m \cdot \left(\frac{T}{T_w} \right)^n \quad \dots \text{for gaseous fluids} \quad \text{Eq 4}$$

where T is the average fluid temperature [K] and T_w is the average wall temperature [K]. For cooling ($T/T_w > 1$) the exponent n is zero, for heating ($1 > T/T_w > 0.5$) n depends on the fluid; for CO_2 , $n = 0.12$.

Remark: In VDI (1994) no comments concerning the influence of the wall temperature on the properties at super-critical pressures are made; in this work equation Eq 3 has been used at super-critical pressures.

A.1.2 Pressure Drop

For the single-phase pressure drop VDI (1994) recommends the implicit form for the friction factor according to Colebrook & White:

$$\frac{l}{f} = -2 \cdot \log \left[\frac{2.51}{Re \cdot \sqrt{f}} + \frac{\epsilon/d}{3.71} \right] \quad \text{Eq 5}$$

where ϵ is the roughness of the tube surface.

A.2 Sub-critical Conditions (Evaporation)

A.2.1 Heat Transfer

Kandlikar (1990) has used for his equation 5246 data points from 24 authors for water, 7 CFCs, nitrogen and neon. The equation is valid for both horizontal and vertical tubes.

The heat transfer coefficient is calculated for convective boiling and nucleate boiling, the larger one is taken as heat transfer coefficient (the 'greater of the two' method).

The heat transfer coefficient is defined by

$$\alpha = \alpha_l [C_1 \cdot Co^{C_2} (25 \cdot Fr')^{C_3} + C_4 \cdot Bo^{C_5} \cdot F_f] \quad \text{Eq 6}$$

where F_f is fluid dependent, C_{1-5} are constants, Fr' the liquid Froude number:

$$Fr' = \frac{\dot{m}^2}{\rho'^2 \cdot g \cdot d} \quad \text{Eq 7}$$

The Boiling number is defined as

$$Bo = \frac{\dot{q}}{\dot{m} \cdot (h'' - h')} \quad \text{Eq 8}$$

and the convection number as

$$Co = \left(\frac{1-x}{x} \right)^{0.8} \left(\frac{\rho''}{\rho'} \right)^{0.5} \quad \text{Eq 9}$$

which in fact is a modified Martinelli parameter.

The single-phase liquid heat transfer coefficient α_l is calculated using the equation of Dittus-Boelter

$$\alpha_l = 0.023 \cdot Re_l^{0.8} \cdot Pr'^{0.4} \cdot \lambda' / d \quad \text{Eq 10}$$

Interesting is the fluid-dependent parameter F_f (Table 10). This parameter can be determined for other fluids also; in this project the procedure has not been carried out for CO_2 . For the calculations

$F_f = 1$ has been used due to similarities of evaporating water (compare constants used in VDI, 1994).

Table 10: The fluid-dependent parameter F_f

Fluid	F_f
Water	1.00
R-11	1.30
R-12	1.50
R-13B1	1.31
R-22	2.20
R-113	1.30
R-114	1.24
R-152a	1.10
N_2	4.70
Neon	3.50

For the constants C_{1-5} there are two columns, one for convective boiling and one for nucleate boiling (Table 11). The greater value of $\alpha_{C_{1-5}, convective}$ and $\alpha_{C_{1-5}, nucleate}$ calculated by Eq 6 has to be used.

Table 11: Constants C_{1-5} for the Kandlikar equation

Constant	convective boiling	nucleate boiling	Remark
C_1	1.1360	0.6683	
C_2	-0.9	-0.2	
C_3	667.2	1058.0	
C_4	0.7	0.7	
C_5	0	0	vertical tubes for any Fr' ; for horizontal tubes with $Fr' > 0.04$
C_5	0.3	0.3	for horizontal tubes with $Fr' < 0.04$

One has to consider that this model gave only acceptable results for low mass fluxes.

A.2.2 Pressure Drop

Thome (1997) recommends the Friedel (1979) correlation for the frictional pressure gradient:

$$\left(\frac{\partial p}{\partial l} \right)_f = \left[\frac{2 \cdot \xi'_0 \cdot \dot{m}^2 \cdot v'}{d} \right] \cdot \phi'^2 \quad \text{Eq 11}$$

where ϕ'^2 is a two-phase multiplier, and ξ'_0 is a friction factor (see Eq 19). The two-phase multiplier is defined as

$$\phi'^2 = G + \frac{3.24 \cdot F \cdot H}{Fr_h^{0.045} \cdot We_h^{0.035}} \quad \text{Eq 12}$$

with the Froude Number (Fr_h) and the Weber Number (We_h) for a (fictitious) homogeneous flow without slip (Eq 16 and Eq 17), and the factors

$$G = (1-x)^2 + x^2 \cdot \frac{v'' \cdot \xi''_0}{v' \cdot \xi'_0}, \quad \text{Eq 13}$$

$$F = x^{0.78} \cdot (1-x)^{0.224}, \text{ and} \quad \text{Eq 14}$$

$$H = \left(\frac{\rho'}{\rho''} \right)^{0.91} \cdot \left(\frac{\eta''}{\eta'} \right)^{0.19} \cdot \left(1 - \frac{\eta''}{\eta'} \right)^{0.7} \quad \text{Eq 15}$$

where ξ'_0 and ξ''_0 are given by Eq 19.

The Froude Number (Fr_h) and the Weber Number (We_h) for a homogeneous flow are defined as

$$Fr_h = \frac{\dot{m}^2}{g \cdot d \cdot \rho_h^2} \quad \text{Eq 16}$$

$$We_h = \frac{\dot{m}^2 \cdot d}{\sigma \cdot \rho_h} \quad \text{Eq 17}$$

where σ is the surface tension and ρ_h is the homogeneous density:

$$\frac{1}{\rho_h} = \left(\frac{x}{\rho''} + \frac{1-x}{\rho'} \right) \quad \text{Eq 18}$$

The Fanning-friction factor can be calculated according to:

$$\xi = \frac{0.079}{\sqrt[4]{Re}} \quad \text{Eq 19}$$

In Eq 11 and Eq 13, the subscript '0' refers to a modified Reynolds Number and friction factor, respectively, which have to be calculated with the properties of the liquid (') or the vapour (") phase and with the total mass flux (\dot{m}), i.e. assuming a single-phase flow at the same mass flux.

For a two-phase flow, the pressure change due to acceleration becomes according to the theorem of momentum:

$$\Delta p_a = \frac{1}{A} \cdot [\dot{M}' \cdot w' + \dot{M}'' \cdot w'']_{in}^{out} = \dot{m}^2 \cdot \left[\frac{x^2}{\rho'' \cdot \varepsilon} + \frac{(1-x)^2}{\rho' \cdot (1-\varepsilon)} \right]_{in}^{out} \quad \text{Eq 20}$$

where ε is the void fraction. Thome (1997) uses the approach of Premoli (1970):

$$\varepsilon = \frac{1}{1 + \left(S \cdot \frac{1-x}{x} \cdot \frac{\rho''}{\rho'} \right)} \quad \text{Eq 21}$$

where S is the slip ratio

$$S = 1 + E_1 \cdot \left(\frac{y}{1 + y \cdot E_2} - y \cdot E_2 \right)^{0.5} \quad \text{Eq 22}$$

with

$$y = \frac{\beta}{1-\beta} \quad \text{Eq 23}$$

$$E_1 = 1.578 \cdot Re_0'^{-0.19} \cdot \left(\frac{\rho'}{\rho''} \right)^{0.22} \quad \text{Eq 24}$$

$$E_2 = 0.0273 \cdot We \cdot Re_0'^{-0.51} \cdot \left(\frac{\rho'}{\rho''} \right)^{-0.08} \quad \text{Eq 25}$$

and the volumetric vapour fraction:

$$\beta = \frac{\rho' \cdot x}{\rho' \cdot x + \rho'' \cdot (1-x)} \quad \text{Eq 26}$$

The Reynolds Number for an assumed liquid flow is defined as

$$Re_0' = \frac{\dot{m} \cdot d}{\eta'} \quad \text{Eq 27}$$

where \dot{m} is the total mass flux. The Weber Number is defined as

$$We = \frac{\dot{m}^2 \cdot d}{\sigma \cdot \rho'} \quad \text{Eq 28}$$